DOKUZ EYLÜL UNIVERSITY

GRADUATE SCHOOL OF NATURAL AND APPLIED SCIENCES

DUAL BAND 23NA/1H, BILATERAL, FLEXIBLE BREAST COIL DESIGN FOR MAGNETIC RESONANCE IMAGING SYSTEMS

by

Büşra KAHRAMAN AĞIR

August, 2021

İZMİR

DUAL BAND 23NA/1H, BILATERAL, FLEXIBLE BREAST COIL DESIGN FOR MAGNETIC RESONANCE IMAGING SYSTEMS

A Thesis Submitted to the
Graduate School of Natural and Applied Sciences of Dokuz Eylül University
In Partial Fulfillment of the Requirements for the Degree of Doctor of Philosophy in Biomedical Technologies, Industrial Ph.D. Program in Advanced Biomedical Technologies

by

Büşra KAHRAMAN AĞIR

August, 2021

İZMİR

Ph.D. THESIS EXAMINATION RESULT FORM

We have read the thesis entitled **"DUAL BAND 23NA/1H, BILATERAL, FLEXIBLE BREAST COIL DESIGN FOR MAGNETIC RESONANCE IMAGING SYSTEMS"** completed by **BÜŞRA KAHRAMAN AĞIR** under supervision of **PROF.DR. KORKUT YEĞİN** and we certify that in our opinion it is fully adequate, in scope and in quality, as a thesis for the degree of Doctor of Philosophy.

....

Prof. Dr. Korkut YEĞİN

Supervisor

....

Assoc. Prof. Dr. Esin ÖZTÜRK IŞIK

Thesis Committee Member

....

Assoc. Prof. Dr. Mustafa Alper SELVER

Thesis Committee Member

....

Prof. Dr. Mustafa SEÇMEN

Examining Committee Member

....

Assoc. Prof. Dr. Merih PALANDÖKEN

Examining Committee Member

Prof. Dr. Özgür ÖZÇELİK

Director

Graduate School of Natural and Applied Sciences

ACKNOWLEDGMENT

I would like to thank my supervisor, Prof. Korkut Yeğin, for his invaluable guidance during the progress of this thesis, his great support for difficulties I faced, making me have the benefit of his precious experiences, and putting ethics above all. Also, I would like to thank Assoc. Prof. Esin Öztürk Işık for sharing her original idea leading to the motivation of this thesis, her guidance and support regarding MRI acquisition and phantom design. Additionally, Assoc. Prof. Mustafa Alper Selver monitored the progress of this thesis and contributed the development of this thesis with his comments and suggestions.

I acknowledge TUBITAK (The Scientific and Technological Research Council of Turkey) for supporting this project under grant number 116E155 and 2214-A International Doctoral Research Fellowship Program. Also, I acknowledge UMRAM (National Magnetic Resonance Imaging Center) at Ihsan Dogramaci Bilkent University, Ankara, Turkey for proton MRI acquisition. Additionally, I thank Prof. Francois Lazeyras from Department of Radiology and Medical Informatics, University of Geneva, Switzerland and Center for Biomedical Imaging (CIBM), Switzerland for sodium MRI acquisition and possibilities provided for working at RF lab. Moreover, I thank DESUM (Dokuz Eylul Industry Application and Research Center) for providing 3D printing, LASER cutting-engraving, and CAM in FABLAB-İZMİR Tınaztepe.

I thank Ahmet Murat Ağır, my husband, for his assistance in CAD/CAM part of this thesis. His and my daughter Neva’s moral support for me, on the other hand, contributed to this thesis at least as much as I did. Other than Murat and Neva, I cannot underestimate the moral support of my whole family.

I thank Olcay Yiğit from Electrical and Electronics Engineering at Ege University, Izmir, Turkey for his assistance in PCB designs and how to use the software programs such as CST and AWR. Furthermore, I thank Basak Bayrambas from ASELSAN, Ankara, Turkey for her support on image processing, such as SNR calculations and filter design.

Büşra KAHRAMAN AĞIR

DUAL BAND 23NA/1H, BILATERAL, FLEXIBLE BREAST COIL DESIGN FOR MAGNETIC RESONANCE IMAGING SYSTEMS

ABSTRACT

A dedicated breast coil plays a significant role in the diagnosis of breast cancer because it can increase the signal to noise ratio (SNR) and therefore the image quality. Since breast coils used in the clinics have a fixed target volume and are not compatible with every patient, the resulting image may be insufficient for an accurate diagnosis. In this thesis, a dual band sodium/proton bilateral breast coil made of a wearable elastic conductive textile (WECOT), which can be compatible with the volume of interest, was described. The design of the breast coil consisted of the production of the conductive textile, the design of a single-channel sodium WECOT breast coil (BC), a two-channel lateral proton WECOT-BC, and a four-channel bilateral proton WECOT-BC. First, a high-conductive silver thread was woven with elastofiber in a weaving machine to produce WECOT with 115 percent elasticity. Phantom studies of the single-channel sodium WECOT-BC demonstrated that SNR was between 30-140 and the coil yielded correct estimations in sodium chloride solutions having different concentrations. A two-channel lateral proton WECOT-BC having a three-stage impedance matching circuit providing broad-band matching was tested in three different sized phantoms, namely, small, medium, and large. While, SNR of the two-channel WECOT-BC was between 60-120 in the small and medium phantom and 60-100 in the large phantom, the minimum resolution of 0.25 mm was obtained. SNR of the four-channel bilateral proton WECOT breast coil was between 100-200 in all three phantoms and the minimum resolution of 1 mm was achieved.

Keywords: Flexible breast coil, elastic, textile, wearable, sodium magnetic resonance imaging, proton magnetic resonance imaging

MANYETİK REZONANS GÖRÜNTÜLEME SİSTEMLERİ İÇİN 23NA/1H ÇİFT BANTLI, BİLETERAL ESNEK MEME BOBİNİ TASARIMI

ÖZ

Özel tasarlanmış meme bobinleri sinyal gürültü oranını (SGO) ve dolayısıyla görüntü kalitesini arttırdığı için meme kanserinin teşhisinde önemli bir rol oynar. Klinikte kullanılan meme bobinleri, sabit hacme sahip olduklarından ve her hasta ile uyumlu olmadıklarından oluşacak görüntünün doğru teşhis için yeterli olmamasına neden olabilmektedir. Bu tezde, boyutu, ilgili hacim ile uyumlu olabilen giyilebilir esnek iletken kumaştan yapılmış bir meme bobini (MB) tanıtılmıştır. MB tasarımı, iletken kumaşın üretimini, tek kanallı sodyum kumaş MB, iki kanallı lateral proton kumaş MB ve dört kanallı bilateral proton MB'nin tasarımından oluşmaktadır. Öncelikle, iletken gümüş iplik dokuma tezgahında elastofiberle dokunarak yüzde 115 esnekliğe sahip iletken bir kumaş elde edilmiştir. Tek kanallı sodyum kumaş MB'nin fantom çalışmaları, SGO'nun 30-140 arasında olduğunu ve bobinin farklı konsantrasyona sahip sodyum klorür çözeltilerinde doğru tahminler verdiğini göstermiştir. Geniş bant uyumlama sağlayan üç katlı empedans uyumlama devresine sahip iki kanallı lateral proton kumaş MB küçük, orta ve büyük olmak üzere üç farklı boyuttaki fantomlarda test edilmiştir. İki kanallı lateral kumaş bobinin SGO'su küçük ve orta fantomda 60-120, büyük fantomda 60-100 arasında iken minimum 0.25 mm çözünürlük elde edilmiştir. Dört kanallı bilateral proton kumaş MB'nin SGO'su üç fantomda da 100-200 arasında olup, her fantomda minimum 1 mm çözünürlük elde edilmiştir.

Anahtar kelimeler: Esnek meme bobini, elastik, kumaş, giyilebilir, sodyum manyetik rezonans görüntüleme, proton manyetik rezonans görüntüleme

CONTENTS

LIST OF FIGURES

Page

LIST OF TABLES

Page

CHAPTER 1

INTRODUCTION

Cancer is a leading cause of death worldwide. While over 10 million people died in the world due to cancer in 2020, breast cancer ranks fifth among cancer deaths worldwide in 2020 and it is the second leading cause of death among women in the USA (American Cancer Society, 2021; World Health Organization, 2021). In addition, the incidence rate of breast cancer worldwide in 2020 has been 2.26 million cases, the highest rate among all the cancer cases, as well as in Turkey and in the USA (American Cancer Society, 2021; Republic of Turkey Ministry of Health, 2021; Siegel, Miller, & Jemal, 2020; World Health Organization, 2021).

Prognosis of breast cancer is determined mostly by the stage of the disease at diagnosis. The highest survival rate is obtained when the disease is at an early stage, localized or regional, while the survival rate decreases steeply in metastatic stage (American Cancer Society, 2021). Clinical breast exam (CBE), mammography, ultrasound (US), and magnetic resonance imaging (MRI) are used in clinical practice for the diagnosis of breast cancer. Mammography or mammography with US which are preferred routinely in clinics, are effective modalities with high sensitivity and specificity. Additionally, MRI is used as an adjunctive method to increase sensitivity for detecting malignancy in cases which mammography and US are inadequate. These cases are young aged women with dense breasts in which the sensitivity of mammography decreases considerably, women with high risk of breast cancer, hormone receptor negative cancer, and staging of invasive lobular cancers, recurrent carcinoma, breast implants, and MR-guided biopsy (Heywang-Kobrunner, Hacker, & Sedlacek, 2013; Mann, Cho, & Moy, 2019).

Early applications of breast MRI were composed of T1 or T2 weighted images that provided limited information to detect carcinoma (Friedrich, 1998; Rankin, 2000). Dynamic contrast-enhanced (DCE) or contrast-enhanced (CE) MRI led to significant increase in sensitivity of breast MRI (Mann, Kuhl, & Moy, 2019; Mussurakis, Buckley, & Horsman, 1997). The technique was based on imaging of gadolinium contrast agent accumulating in breast stroma which was undergone angiogenesis (Mann, Kuhl, et al., 2019). Other than CE-MRI, to date multiparametric MRI including diffusion weighted imaging (DWI), proton (^{1}H) MR spectroscopy, sodium imaging (^{23}Na MRI), Phosphorus Spectroscopy (31P MRS), Chemical Exchange Saturation Transfer (CEST) Imaging, Blood Oxygen Level-Dependent (BOLD) MRI, and Hyperpolarized MRI (HP MRI) offers insight to the hallmarks of cancer. The process transforming a normal cell into a cancer cell includes six hallmarks, namely, maintaining growth signal, insensitivity to antiproliferative signal, resisting apoptosis, infinite replicative capability, inducing angiogenesis, and metastatic dissemination (Hanahan & Weinberg, 2000). Ductal Carcinoma In Situ (DCIS) is a malignant proliferation of ductal epithelial cells of breast, whose malignant potential leads to invasive cancer (Greenwood, Wilmes, Kelil, & Joe, 2020). While mammographic presentation of DCIS is microcalcification, mass or architectural distortion, DCIS could be detected as nonmass enhancement (NME), a mass or focus on MRI (Greenwood et al., 2020).

Sodium has significant roles in human metabolism in terms of sustaining homeostasis, pH setting, participating in heart activity, transmission of nerve impulses, and muscle contraction (Madelin, Lee, Regatte, & Jerschow, 2014). Na+/K+-ATPase, known as sodium–potassium pump, maintains the intracellular sodium concentration and the extracellular sodium concentration between 10-15 mM and 140-150 mM, respectively. The disruption of sodium–potassium pump resulting from over demand of ATP due to the proliferation of malignant cells in breast leads to a malfunction of this gradient, and thus an increase in tissue sodium concentration compared to glandular tissue (Ouwerkerk et al., 2007).

The effectiveness of multiparametric MRI in the diagnosis of breast cancer and monitoring of treatment response relies on the image quality, and consequently signal intensity (Marino, Helbich, Baltzer, & Pinker-Domenig, 2018). A dedicated breast coil can provide significant improvements in signal-to-noise ratio (SNR) and image quality, as well as enabling bilateral imaging of breasts yielding a comparison between two (Ojeda-Fournier, Choe, & Mahoney, 2007). Additionally, such breast coil does not include the organs causing a motion artifact such as heart and lung in the resulting image (Wolfman, Moran, Moran, & Karstaedt, 1985). Breast coils are used in either transmit mode (excitation) or receive mode.

First designs of breast coils had single channel and surface or saddle geometry (Hornak, Szumowski, & Bryant, 1987; Mcowan & Redpath, 1987; Wolfman et al., 1985). Along with that the coil arrays were depicted, new approaches regarding multichannel coils were manifested (Insko, Connick, Schnall, & Orel, 1997; Kaggie et al., 2014; Nnewihe et al., 2011). Breast coil arrays taking part in ultra-high field MRI provided high-resolution breast CE-MRI, an increase in diagnostic accuracy and image quality (Brown et al., 2014; By et al., 2014; Kim et al., 2017; Marino et al., 2018; McDougall et al., 2014). Moreover, dual band $^{23}Na/^{1}H$ breast coils (Ianniello et al., 2017; Kaggie et al., 2014) have been gaining attention in terms of their contribution to improvements of sensitivity and specificity of breast MRI.

Although introduced breast coils had considerable benefits in breast imaging, they were not compatible with different breast sizes. Indeed, fixed sized breast coils, are used in clinical practice of breast MRI. When the size of the patient's breast is not compatible with the corresponding breast coil, filling factor of the coil is affected, consequently, image quality is degraded. In addition, even though frequency shift resulting from different loading can be somewhat compensated by the low noise amplifier (LNA), images of trapped breasts inside of the coil may not provide sufficient diagnostic information such as peripheral bright signal because of breast touching the coil, flattening of the tissue, or delay in contrast arrival due to pinching of blood vessels (Ojeda-Fournier et al., 2007). Other than image quality and diagnostic issues, adaptability of the coil size to the target breast size is desired since the depth of the magnetic field penetration is limited by the diameter of the coil.

Proposed screen printed coils (Corea et al., 2016; Hancu et al., 2016; Winkler et al., 2019) and flexible (Frass-Kriegl et al., 2018; Vasanawala, 2017) RF coil arrays have demonstrated bendable and conformal features instead of being size adjustable. A conventional but size adaptable copper (Cu) coil has been introduced (B. Zhang et al., 2019). Recently, wearable detector arrays composed of liquid metal (Port et al., 2020), coaxial cable (B. Zhang, Sodickson, & Cloos, 2018), Cu braid (Nordmeyer-Massner, De Zanche, & Pruessmann, 2012), and elastomer coils (Port, Luechinger, Brunner, & Pruessmann, 2021) have been presented.

To date, the usage of electro textiles of conductive textiles in the form of Cu wire covered with silk or polyamide, sewing the components onto a fabric with a conductive thread, and screen printing (Grabham, Li, Clare, Stark, & Beeby, 2018). Conductive thread based MR coils (Vincent & Rispoli, 2020; D. S. Zhang & Rahmat-Samii, 2017) have put the applicability of wearable electro-textiles forward. These coils have been created by sewing a conductive thread onto a non-conductive fabric. On the other hand, the conductive thread-based coils which were created this way; 1) had a very short width limited by the conductive thread itself, which was undesirable in transmit mode, 2) may undergo to damages and cuts, which might lead to an open circuit, and 3) had a circuit hard to intervene such as adding or removing a component and changing the length of the coil.

The goal of this thesis was to design a dual band bilateral ^{23}Na/^{1}H size changeable breast coil at 3 T. The first chapter introduced the production technique of the conductive textile and implementation of an elastic loop coil using this textile. The second chapter and third chapter presented a wearable elastic conductive textile (WECOT) ^{23}Na breast coil and a four-channel bilateral WECOT breast coil, respectively. Finally, the fifth chapter proposed a design of a low noise amplifier (LNA) which can operate both at sodium and proton frequency.

CHAPTER 2

WEARABLE AND ELASTIC LOOP COIL

2.1 Introduction

The target volume plays a critical role in determining the geometry of radiofrequency (RF) coils. In case of breast coils, mostly semi-spherical structures (By et al., 2014; Kaggie et al., 2014) or cylindrical structures (Brown et al., 2014; Hornak et al., 1987; Kim et al., 2017; McDougall et al., 2014; Wolfman et al., 1985) are employed. Additionally, although the breasts sizes might largely vary between the individuals, often fixed medium-sized breast coils are used for all in the clinics. When the patient's breast size is not compatible with the breast coil in use, breasts would either be trapped in the coil or the coil loading has to be promoted by other materials, such as supportive sponges. Unsatisfactory filling factor is directly related to the impedance matching and signal-to-noise ratio (SNR), hence image quality. Additionally, even though the frequency shift resulting from a low filling factor could be somewhat compensated by image post-processing, MR images of larger breasts may have artifacts that might prevent a proper diagnosis, such as peripheral bright signal due to coil touching the breast, flattening of the tissue, or delay in contrast arrival due to pinching of blood vessels (Ojeda-Fournier et al., 2007). Another disadvantage of fixed-size coils is that the depth of magnetic field penetration is usually limited by the diameter of the coil (Wang, Reykowski, & Dickas, 1995). Ideally, the coil diameter should be adaptable to the breast size.

With the recent advances in on-body communications and sensors, conductive textiles have been heavily utilized in the form of screen printing, sewing conductor thread, and copper (Cu) wire covered with silk (Grabham et al., 2018). In MRI applications, flexible coils have also been demonstrated, in which, the flexibility referred to bendability, but, they all have had fixed target volumes (Corea et al., 2016; Frass-Kriegl et al., 2018; Hancu et al., 2016; Winkler et al., 2019; T. Zhang et al., 2016). A size changeable conventional coil, on the other hand, have provided adjustability with different sized phantoms (B. Zhang et al., 2019). Textile (D. S.

Zhang & Rahmat-Samii, 2017) and wearable liquid metal coils (Port et al., 2020) have also been proposed as alternative approaches to flexibility with limitations.

In this chapter, a single channel receive-only elastic textile proton MR coil was designed. The target region of interest (ROI) was determined as breast. The textile coil could expand and retract, while preserving its maximum loading factor and a fixed impedance. A preliminary version of this work was reported in conference proceeding (B. Kahraman-Agir, Bayrambas, B., Yegin, K., Ozturk-Isik, E., 2019). Coil measurements and phantom studies were conducted to evaluate the image quality and the flexibility of the coil.

2.2 Methods

2.1.1 Simulations and 3D Printing

Three phantoms, namely, small (S-P), medium (M-P), and large (L-P) were designed in a 3D CAD software (ThinkDesign, DPT Corporate, Italy) and printed in a 3D printer (Ultimaker2, Netherlands). Dimensions of phantoms were gradually 50% greater than the previous size (Table 2.1). Accordingly, small, medim, and large loop coils (Fig. 2. 1a) whose material was copper (Cu) were created in a 3D electromagnetic simulation software (Computer Simulation Technologies, CST, AG, Germany). The size of the coils were compatible with S-P, M-P, and L-P. Each coil was tuned at 123.2 MHz with a tuning capacitor connected serially (operating resonance frequency at 3T) after their inductance was calculated. The value of tuning capacitor for small, medium, and large coil was determined as 13pF, 6pF, and 3pF, respectively. Three oil phantoms compatible with S-P, M-P, and L-P were also created to load the coils. Each coil was loaded by the corresponding oil phantom. Their B_1^- field (reception field) were calculated at x=0 and z=0 plane (Fig. 2.1b-d) for sagittal and axial cuts, respectively.

Table 2.1 Dimensions of the phantoms where A,B, and C were radius of x-axis, radius of y-axis, and height, respectively

Phantom	A (mm)	B (mm)	C (mm)	Volume (mL)
S-P	75	100	87	276
M-P	112	150	132	986
L-P	150	200	177	2435

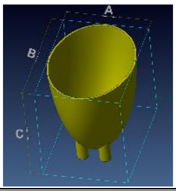

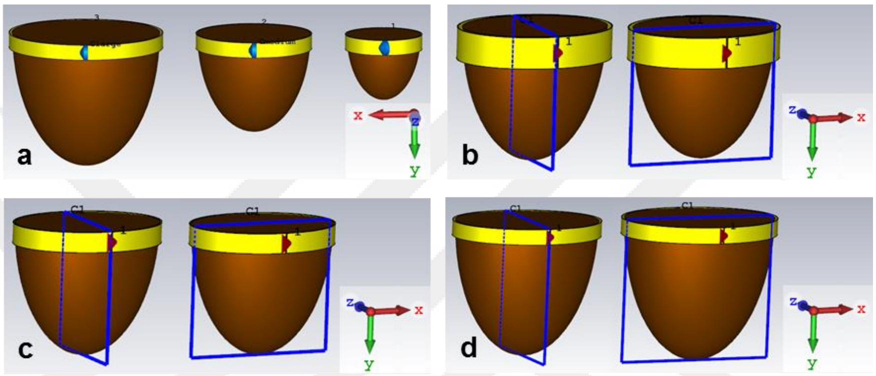

Figure 2.1 Simulation studies. (a) Large, medium, and small loop coils from left to right, respectively. x=0 and z=0 planes of (b) small, (c) medium, and large (d) loop coil (Personal archive, 2018)

2.1.2 *Two-stage Low Noise Amplifier*

2.1.2.1 *Simulations*

The first stage of LNA was designed in an electronic design automation software (AWR, National Instruments, USA) based on SAV 581+ (Mini-Circuits Technologies, Scientific Components Corp., USA) transistor considering characteristics in Table 2.2. |S11|, |S22|, |S21|, noise figure (NF), and 1 dB compression point were calculated. Stability was checked from 10 MHz to 12 GHz. Similarly, two-stage LNA were created in AWR. |S11|, |S22|, |S21|, and noise figure (NF) were calculated. Also, stability was calculated from 10 MHz to 12 GHz.

2.1.2.2 *Experiments*

Printing circuit board (PCB) layout (Fig. 2.2) of two-stage LNA (Fig. 2.3) was prepared in AWR. Since the MR scanner (Siemens Magnetom Trio, Siemens Healthineers, Germany) provided 10 V of DC voltage along with a RF signal, a regulator (TPS715A, Texas Instruments, USA) was used to obtain 4.4 V DC voltage (Fig. 2.4). C1=C2=C3=C4= 560 pF (S111DUE, Johanson Technology Inc., USA), L1=L2= 12 nH (1008HT, CoilCraft, USA) were applied. R1, R2, R3, and R4 were 830 Ω, 390 Ω, 390 Ω, and 830 Ω, respectively.

Table 2.2 The desired characteristics of the first stage of LNA

Properties	**Value**
Input and Output Impedance	50 Ω and 50 Ω
Input Return Loss |S11|	<-10 dB
Output Return Loss |S22|	<-10 dB
Noise Figure (NF)	< 2 dB
Gain |S21|	>15 dB
1dB compression point	>-15 dBm

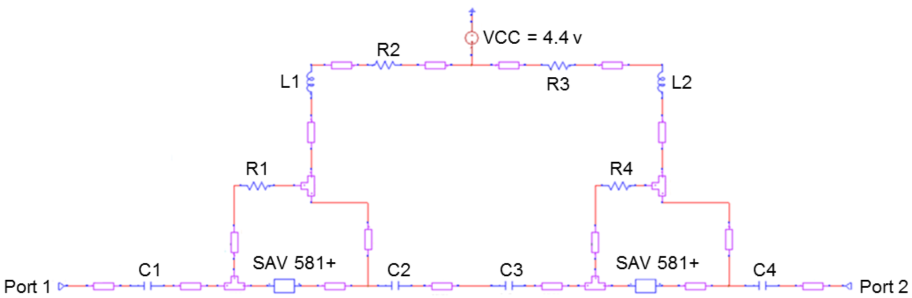

Figure 2.2 AWR schematic of two-stage LNA where C1=C2=C3=C4= 560 pF, R1, R2, R3, and R4 were 830 Ω, 390 Ω, 390 Ω, and 830 Ω, respectively, L1=L2= 10 nH. Properties of FR4 were relative permittivity, ϵ_r= 4.5, height, H= 1 mm, thickness, T= 0.035 mm, ρ= 1, tangential loss Tand= 0.02

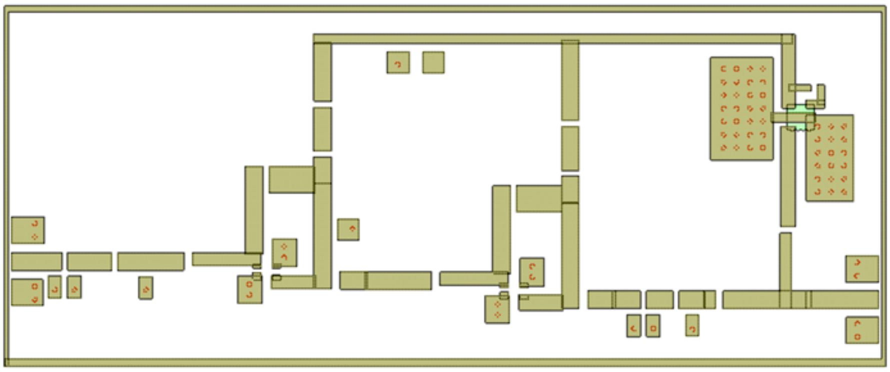

Figure 2.3 PCB design of LNA created in AWR. Green rectangle on the right corner of the figure represents the regulator

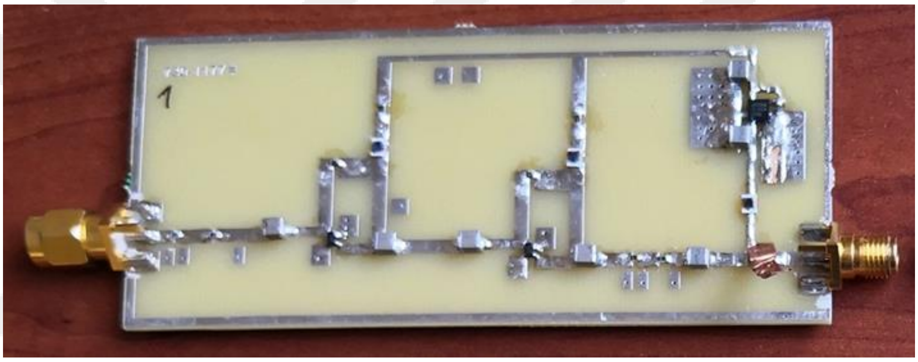

Figure 2.4 PCB of two-stage LNA

2.1.3 Conductive Threads

Four conductive threads, stainless steel (Sparkfun USA), high conductive silver (Statex, Germany), carbon (Cemre Iplik, Turkey) and silisium (Teksmer, Turkey) were examined in terms of their MR compatibility, resistance, and ability to be woven (Table 2.3). The silver thread was superior to the others considering its low resistance and to be easy to woven.

2.1.4 Conductive Textiles

Three different weaving methods were applied to the silver thread. Firstly, the silver thread was woven as rib, so that the textile became stretchable because of the weaving technique (Fig. 2.5a). Secondly, the silver thread was covered around an elastofiber to create an elastic thread. Afterwards, the elastic conductive silver thread was woven (Fig. 2.5b). Thirdly, weaving process was fed with a lyrca coil while the silver thread was woven as rib (Fig. 2.5c). All textiles were 20 mm-wide. The weaving procedure was conducted in a weaving machine (NSSG 122, Shima Seiki, Japan). The percentage of elasticity (2.1) of the first, the second and the third method was 28.6%, 83%, and 115.5%. The conductive textile produced in the third method was determined as the source of the wearable loop considering its high elasticity and softness.

Table 2.3 The properties of conductive threads

Thread Type	MRI compatibility	Resistance	Ability to be woven
Stainless steel	✗	28 Ω/ft	✓
Carbon	✓	1 MΩ/m	✗
Silisium	✓	Couldn’t be measured	✓
Silver	✓	10-30 Ω/m	✓

$$Elasticity\ (\%) = \frac{Final\ length - initial\ length}{initial\ length} \times 100 \tag{2.1}$$

2.1.5 Connection Circuit

Since the silver thread contained polyamide 6.6, it could not be soldered like any other circuit components. Therefore, a connection circuit was required in order to combine the ends of the loop coil and solder circuit components, such as capacitors, diodes. etc. A 15 mm-wide, 40 mm-long FR4 printed circuit board (PCB) was designed (Fig. 2.6a). Multiple holes on both sides of the connection circuit enabled the circuit to be sewn on the textile (Fig. 2.6b). The silver thread was used in the sewing procedure which was manually employed.

Figure 2.5 The conductive textiles made from the silver thread by (a) the first, (b) the second, and (c) the third weaving technique (Personal archive, 2018)

Figure 2.6 (a) Connection circuit. (b) Connection circuit sewn onto the conductive textile (Personal archive, 2018)

2.1.6 Wearable Textile Loop Coils

230 mm-long and 320 mm-long conductive textile were cut. Each piece was formed into a loop by combining both ends with a connecting circuit. Because the loop coil made from 230 mm-long conductive textile was compatible with both S-P and M-P, it was called S-M coil (Fig. 2.7a). Likewise, the loop coil created by 320 mm-long conductive textile was compatible with both M-P and L-P, thus it was called M-L coil

(Fig. 2.7b). DC resistance of S-M coil and M-L coil was 0.94 Ω and 1.034 Ω, respectively (Digital Multimeter, Rigol, DM3058).

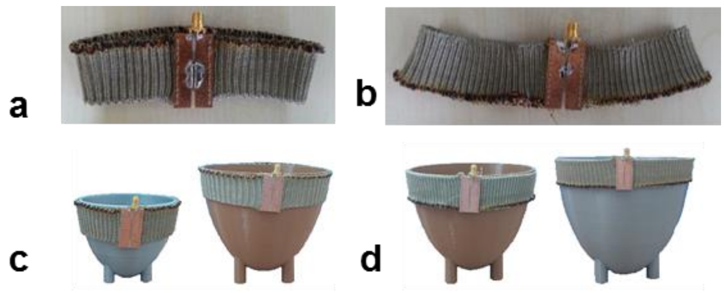

Figure 2.7 Wearable loop coils. (a) S-M coil, (b) M-L coil, (c) S-M coil placed on S (left) and M (right), and (d) M-L coil placed on M (left) and L (right) (Personal archive, 2018)

Inductance of S-M coil when it wore S-P (L_S) and M-P (L_{M1}) was measured in a Network Analyser (R&S ZVL). Similarly, inductance of M-L coil when it was placed on M-P (L_{M2}) and L-P (L_L) was measured. In order for a system to be tuned by a capacitor, the imaginary part of Z11 must be or almost zero, therefore the input impedance of the circuit is minimized. It should be noted that tuning is an empirical process, hence the tuning capacitance was altered in bench measurements considering the imaginary part of Z11. Each coil was tuned by a tuning capacitor at 123 MHz (operating Larmor frequency at 3 T). C_M (Fig. 2.8) of S-M coil and M-L coil was 190 pF and 220 pF, respectively. The matching of the S-M coil was achieved by C_1 (220 pF) and L_1 (6.8 nH). No further adjustments related to tuning were made when the S-M coil was placed on S-P and M-P. C_1 and L_1 of the matching of the M-L coil were 220 pF and 7.5 nH, respectively. Likewise, no further adjustments were made on the tuning of the matching circuit when M-L coil was placed on M-P and L-P.

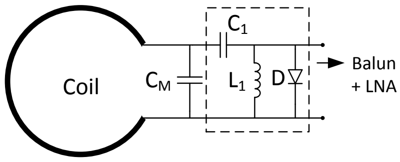

Figure 2.8 The matching network and trap circuit before the balun and low noise amplifier (LNA)

The quality factors of the coils were calculated (Doty, Connick, Ni, & Clingan, 1988) when the phantoms were empty ($Q_{unloaded}$) and loaded (Q_{loaded}) with corn oil filled phantoms. Each coil had two Q_{loaded} values since it was compatible with two phantoms.

2.1.7 Conventional Loop Coils

Two copper loop coils (Fig. 2.9) with circumferences of 534 mm (ConvM) and 691 mm (ConvL) were created for reference of S-M coil and M-L coil, respectively. The ConvM was tuned with a capacitor connected in serial (C_T, 3.8 pF) and matched with a shunt capacitor (C_M, 110 pF). C_T and C_M of the ConvL were 2.2 pF and 100 pF, respectively. $Q_{Unloaded}$ and Q_{Loaded} were calculated when the coils were unloaded and loaded with corn oil. While ConvM was filled with S-P and M-P, ConvL was filled with M-P and L-P.

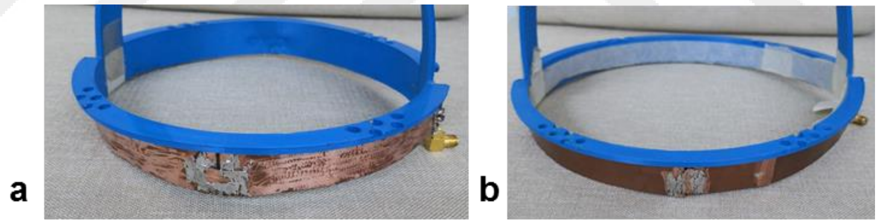

Figure 2.9 Conventional copper loop coils. (a) ConvM and (b) ConvL (Personal archive, 2021)

2.1.8 Resolution Plate and Phantom Studies

Two resolution plates, one was for S-P and the other was for M-P and L-P, were designed in Visi CAD/CAM (Vero Software, United Kingdom) and engraved in a CNC Router (TTMAK, Turkey). Circular hole diameters ranged from 6 mm to 20 mm and rectangular holes ranged from 6x6 to 10x20 mm^2.

Phantom studies were conducted at a 3 T MRI system (Siemens Magnetom Trio, Siemens Healthineers, AG, Germany). The phantoms were filled with corn oil to mimic the fat tissue in breasts (By et al., 2014; Pethig & Kell, 1987), along with the resolution plate was placed inside. Since both loop coils were compatible with two different phantoms, two sets of images were acquired for each of them, such that MR images of S-P and M-P were acquired by S-M coil, and similarly, MR images of M-P and L-P were obtained by M-L coil. The scan parameters for T2-weigted turbo spin echo (TSE) sequence were TR/TE=5410/85 ms , FOV=160x160 mm, and slice thickness= 3 mm. The regions close to the coil were utilized in SNR calculations.

2.2 Results

2.2.1 Simulation

The simulated inductances of the small, medium, and large loop coils were 128 nH, 270 nH, and 507 nH, respectively. The intensity of B_1^- field created by the coils (Fig. 2.10) decrease gradually as the size of the phantom increases, which was an expected result considering the magnetic field intensity decreased at the point away from the current source. The highest B_1^- field (Fig. 2.10a,b) was created by small loop coil. In addition, non-uniform B_1^- fields resulted from the coil geometry.

2.2.2 Two-stage Low Noise Amplifier

2.2.2.1 Simulations

Simulated |S11|, |S22|, |S21|, and NF of the first stage of LNA at 32.6 MHz were -16.15 dB, -13.83 dB, 22.38 dB, and 0.3968 dB, respectively (Fig. 2.11). Likewise, simulated |S11|, |S11|, |S22|, |S21|, and NF of the first stage of LNA at 123.2 MHz were -15.75 dB, -14.89 dB, 21.87 dB, and 0.4151 dB, respectively (Fig. 2.11). Stability from 10 MHz to 12 GHz is higher than 1 (Fig. 2.12). Simulated |S11|, |S22|, |S21|, and NF two-stage LNA at 32.6 MHz were -22.7 dB, -20.4 dB, 44.5 dB, and 0.399 dB, respectively (Fig. 2.13). Similarly, simulated |S11|, |S22|, |S21|, and NF of the first stage of LNA at 123.2 MHz were -20.9 dB, -20.1 dB, 43.7 dB, and 0.418 dB, respectively (Fig. 2.13). Stability checking from 10 MHz to 12 GHz of both the first stage of LNA and two-stage LNA was higher than 1 (Fig. 2.12 and 2.14), which indicated any signal within this frequency range could not interfere.

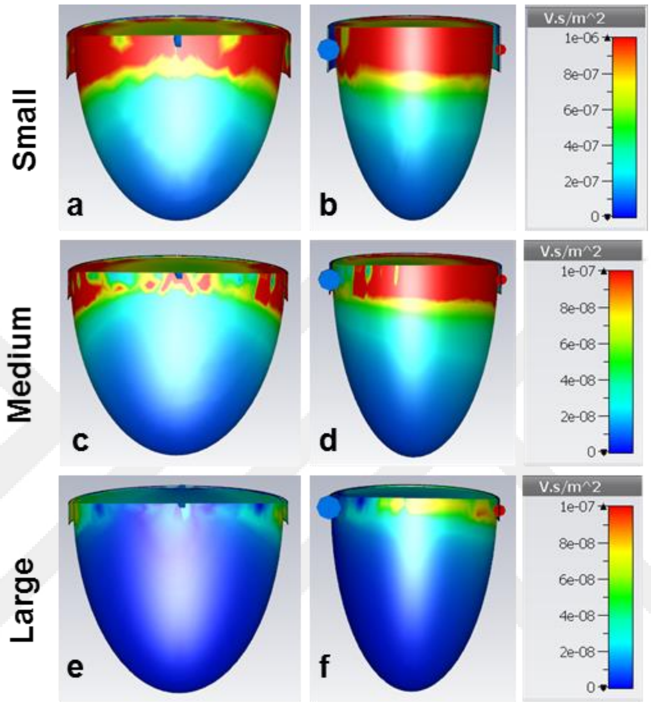

Figure 2.10 The simulated B_1^- fields of small (top row), medium (in the middle), and large (bottom row) loop coils. B_1^- field at z=0 plane of (a) small loop coil, (c) medium loop coil, (e) large loop coil. B_1^- field at x=0 plane of (b) small loop coil, (d) medium loop coil, (f) large loop coil

2.2.2.2 *Experiments*

Measured |S11|, |S22|, and |S21| of two-stage LNA at 32.6 MHz were -17.2377 dB, -21.1553 dB, and 37.3859 dB, respectively (Fig. 2.15). Likewise, measured |S11|, |S22|, and |S21| of two-stage LNA at 123.2 MHz were -14.7132 dB, -21.2398 dB, and 37.1895 dB, respectively (Fig. 2.15).

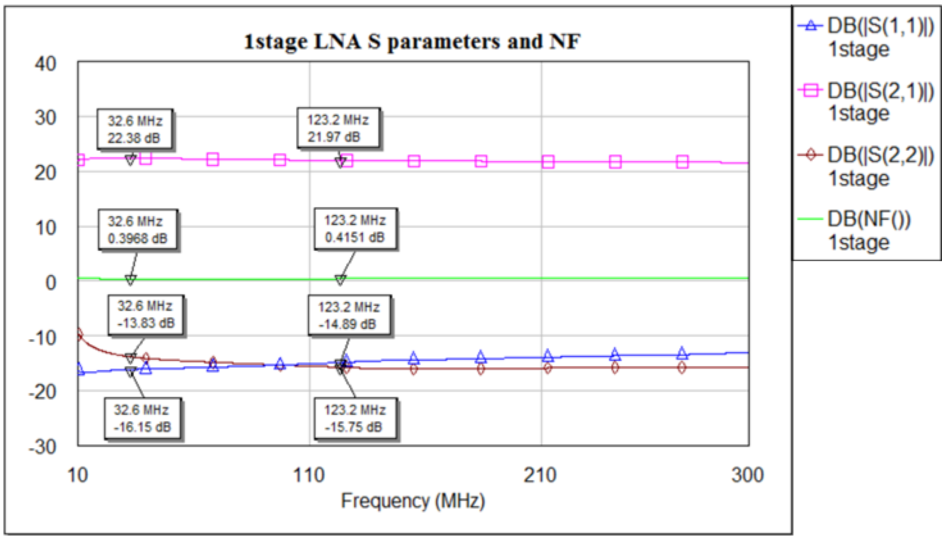

Figure 2.11 Simulated |S11|, |S22|, |S21|, and NF of the first stage of LNA

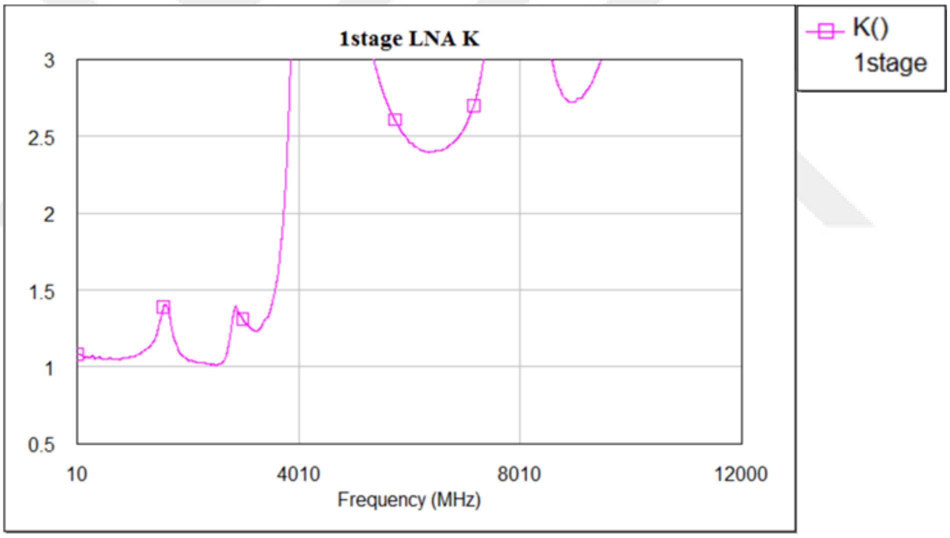

Figure 2.12 Stability of the first stage of LNA

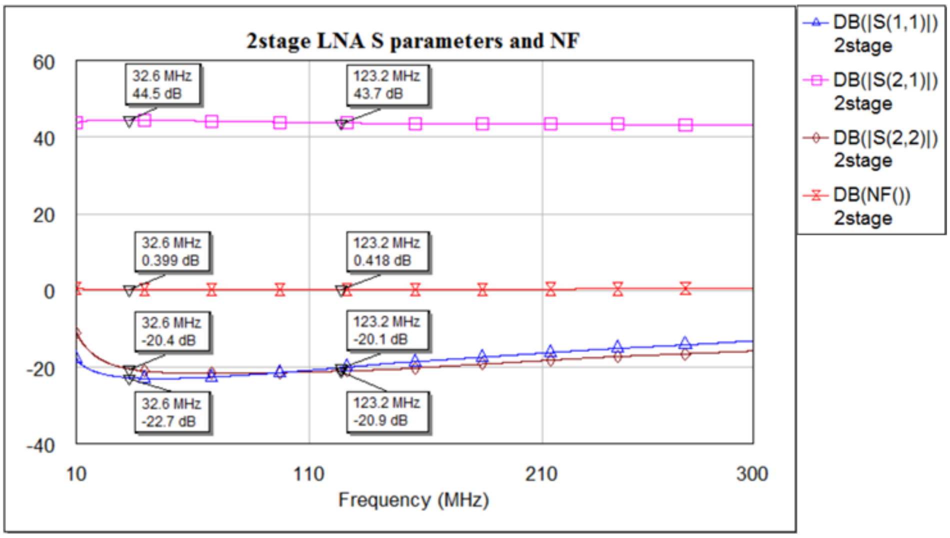

Figure 2.13 Simulated |S11|, |S22|, |S21|, and NF of two-stage LNA

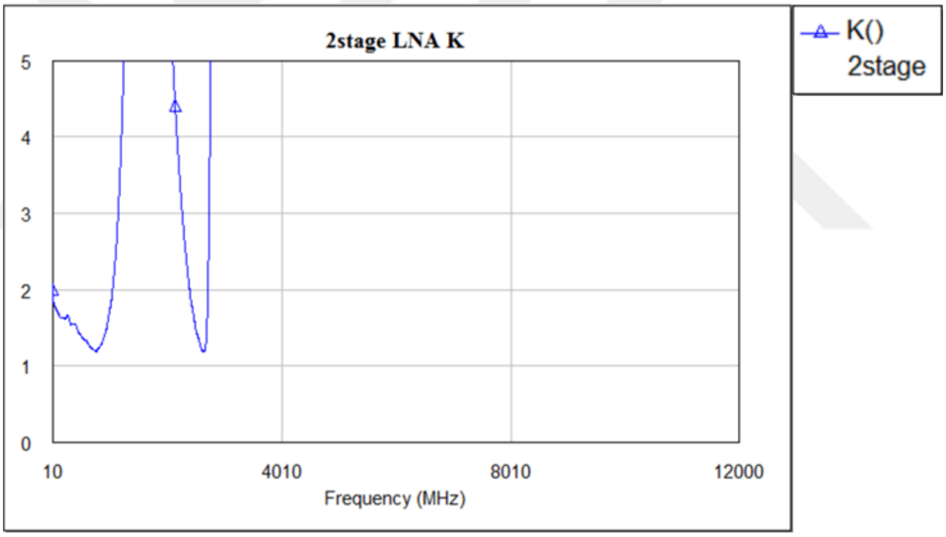

Figure 2.14 Stability of two-stage LNA

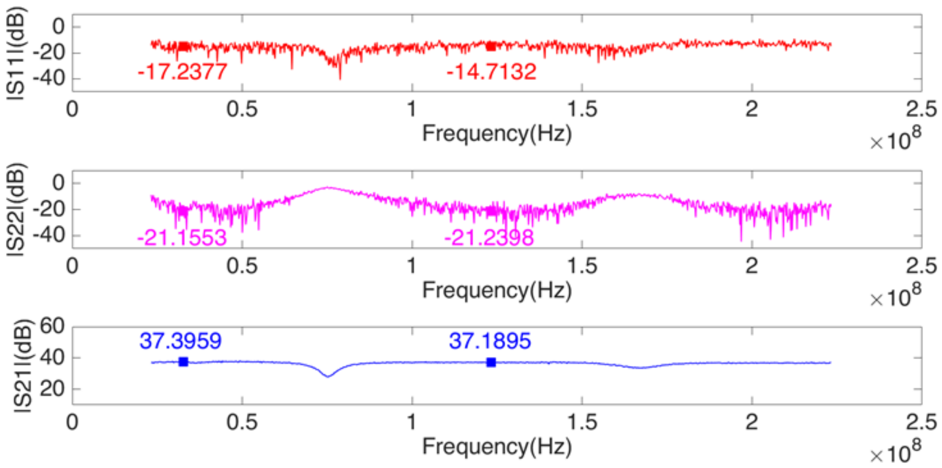

Figure 2.15 Measured |S11|, |S22|, and |S21| of two-stage LNA

2.2.2.3 Bench Measurements

L_S, L_{M1}, L_{M2}, and L_L were 130 nH, 320 nH, 340 nH and 900 nH, respectively. Measured inductances of textile loop coils corresponded with the simulated inductances of Cu-based loop coils, except the measured inductance of M-L coil on L-P.

|S11| of the matching of the S-M coil on S- and M-P were -17 dB and -24 dB, respectively (Fig. 2.16a,b). |S11| of the matching of M-L coil on M-P and L-P were -18 dB and -14 dB, respectively (Fig. 2.16c,d). Contrary to conventional coils where one or more series capacitors can be placed on the coil with a shunt capacitor at the coil input, a shunt capacitor (C_M) and a serial capacitor (C_1) (Fig. 2.8) were used for broad band matching of textile coil; thus, the matching could be retained although the different sized phantoms were used. The drawback of this approach was relatively non-uniform current distribution along the coil. If series capacitor were to be used, the phase shift along the coil would not have been compensated.

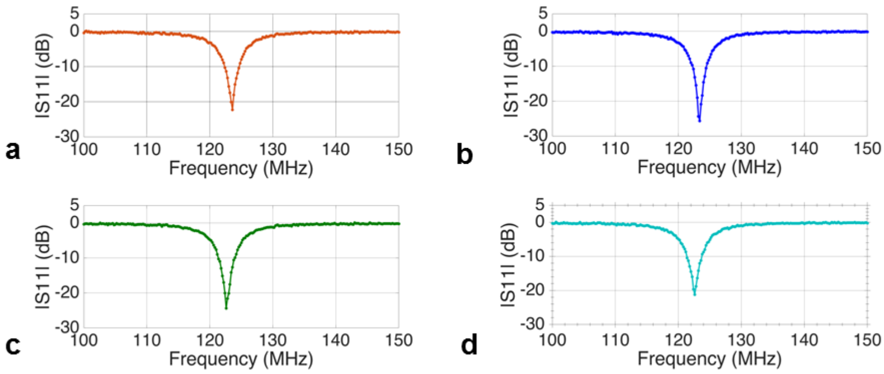

Figure 2.16 Reflection coefficient plots of (a) S-M coil on S-P, (b) S-M coil on M-P, (c) M-L coil on M-P, (d) M-L coil on L-P phantom

Table 2.4 Q factor calculations

Coil	**Phantom**	$\mathbf{Q_{Unloaded}}$	$\mathbf{Q_{Loaded}}$	$\mathbf{Q_{Ratio}}$
S-M	S	124	109	1.13
S-M	M	206	154	1.34
M-L	M	154	123	1.25
M-L	L	153	102	1.5
ConvM	S	293	241	1.2
ConvM	M	293	201	1.46
ConvL	M	535	382	1.4
ConvL	L	535	382	1.4

Low Q_{Ratio} ($Q_{Unloaded}/Q_{Loaded}$) of the textile coils and the conventional coils was due to the low conductivity of the oil (Table 2.4) (Brown et al., 2013; Frass-Kriegl et al., 2018; Pethig & Kell, 1987; Vincent & Rispoli, 2020). However, it is apparent that as the target volume increases, Q_{Loaded} decreases; therefore, the filling factor increases, as expected. Compared to conventional Cu-only coil, textile coil had almost twice more ohmic losses which also resulted in lower Q-ratios.

2.2.3 Phantom Studies

Acquired phantom images were given in Fig. 2.17. It was expected that the SNR results (Table 2.5) of S-M coil on M-P was the highest among the sagittal images owing to its highest Q_{Ratio} (Table 2.4). The highest mean SNR on axial plane obtained when S-M coil was on S-P despite its low Q_{Ratio} was by virtue of the small ROI. S-M coil and M-L coil had similar SNR results when placed on M-P, which was verified by their similar Q_{Ratio} results. Based on measured Q-values and (2.2), the textile coil is expected to perform 1.5-2 dB worse than its Cu-only counterpart under the same filling factor.

Although the mean SNR values of the textile coils were lower than those of typical all-metal counterparts, the holes in the resolution plates could be easily distinguished. The inplane resolution of the images was 0.39 mm/pixel.

Table 2.5 SNR calculations

Plane	Coil	Phantom	Near
Axial	S-M coil	S	70
	S-M coil	M	19
	M-L coil	M	16
	M-L coil	L	11
Sagittal	S-M coil	S	24
	S-M coil	M	25
	M-L coil	M	22
	M-L coil	L	10

$$SNR \propto \frac{\omega^2 B_1}{\sqrt{R_{coil} + R_{sample}}} \tag{2.2}$$

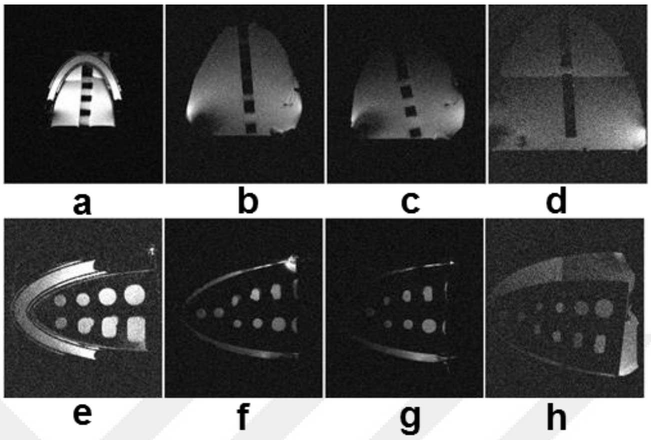

Figure 2.17 The MR images of the phantoms acquired with the elastic textile coils. The axial slices of (a) S-P acquired by S-M coil, (b) M-P by S-M coil, (c) M-P by M-L coil, and (d) L-P by M-L coil. The sagittal slices of (e) S-P acquired by S-M coil, (f) M-P by S-M coil, (g) M-P by M-L coil, and (h) L-P by M-L coil (Personal archive, 2018)

2.3 Conclusion

Here, two wearable and elastic textile loop coils made from a stretchable textile were presented. The method introduced here differs from the other approaches (Corea et al., 2016; Frass-Kriegl et al., 2018; Grabham et al., 2018; Hancu et al., 2016; Nordmeyer-Massner et al., 2012; Port et al., 2020; Vasanawala, 2017; Vincent & Rispoli, 2020; Winkler et al., 2019; D. S. Zhang & Rahmat-Samii, 2017) in terms of the production of the coil material and the degree of elasticity. Also, the weaving process enabled the width of the textile and the percentage of the elasticity to be predetermined. In addition, high elasticity of the conductive textile minimized the limitations regarding the adjustability of the target volume and the coil size. Moreover, the fact that one matching circuit was adequate to maintain the matching even though the inductance altered when the textile coil was placed on its target phantoms is another significance of this study.

This study had some limitations. Inability of being soldered of the textile entailed the use of a conventional component, such as a connection circuit. The size of the connection circuit depended on the width of the textile and the case of the capacitors, so it had to be custom-made. Since using the connection circuits led to a textile-PCB based structure, the number of the connection circuit used in the textile coil had to be minimized in order to create a textile dominant structure. This might not seem as a problem when the textile coil is used in the receive mode, but, if the number of the tuning capacitors increased such as in the transmit mode, the textile coil may lose its elasticity due to the increased number of connection circuit. Compared to Cu-only conventional coil, textile coil had almost twice ohmic losses which led to SNR reduction in MRI experiments. Low mean SNR values Q-ratios may seem a performance compromise, which may have resulted from the inhomogeneous B_1^- field due to the simple coil geometry coupled with matching network, and fast T2 relaxation of oil, which was placed inside the phantoms. Further enhancements of elastic coil concerning the geometry and the number of channels could be carried out to overcome these drawbacks for clinical applications.

CHAPTER 3

TRANSCEIVER ^{23}NA WECOT BREAST COIL

3.1 Introduction

Early detection of breast cancer plays a crucial role in execution of treatment strategies. Contrast enhanced magnetic resonance imaging (MRI) enables diagnosis of angiogenesis present in invasive tumors and ductal carcinoma in situ (DCIS) (Heywang-Kobrunner et al., 2013). Furthermore, sodium (^{23}Na) MRI offering insight into the physiology and metabolism of suspicious lesions has been gaining attention to prevent false-negative diagnoses (Madelin et al., 2014). Disruption of sodium-potassium pump in malignant breast tumors leads to an increase in intracellular sodium concentration (Madelin et al., 2014; Ouwerkerk et al., 2007). The changes in tissue sodium concentration could be detected by a dedicated ^{23}Na radiofrequency (RF) coil, although the MR signal of sodium is quite low (Jacobs et al., 2011; Jacobs et al., 2004; Ouwerkerk et al., 2007).

Hemispherical (By et al., 2014; Kaggie et al., 2014) or cylindrical structures (Brown et al., 2014; McDougall et al., 2014) are usually preferred in breast RF coil designs, since they are more suitable to breast anatomy. On the other hand, the breast size is independent of age and weight; therefore, a predetermined target volume may cause some limitations. An incompatibility between the patient's breast and the breast coil size may alter the loading factor, and therefore the resonance frequency. Resultant coil performance may also deteriorate the signal-to-noise-ratio (SNR) and the image quality. Additionally, larger breasts may be squeezed in the coil housing that might result in alterations of the time-signal intensity curve shapes, consequently, affecting the diagnosis of malignant lesions or higher signal intensities at locations touching the coil (Kuhl et al., 1999). Since the filling factor is the ratio of the magnetic energy stored in the sample to the total magnetic energy stored in the coil (Vaughan & Griffiths, 2012), the adaptability of the coil diameter to the target breast size is ideally desired because the depth of the magnetic field penetration is limited by the diameter of the coil. Therefore, a size adjustable coil would be a key advancement not only for the image quality and proper diagnosis, but also for patient comfort.

Flexible MR coils proposed recently (Corea et al., 2016; Frass-Kriegl et al., 2018; Hancu et al., 2016) had bendable and conformal properties rather than being size adjustable. An inflexible but size changeable copper (Cu) coil's adaptability (B. Zhang et al., 2019) has been demonstrated in different sized phantoms. Additionally, a wearable liquid metal coil (Port et al., 2020) and a high-impedance resonant coaxial array-glove coil (B. Zhang et al., 2018) have brought new interpretations to flexibility.

Recent progress in on-body communications and sensors facilitated the usage of conductive textiles in the form of Cu wire covered with silk or polyamide, sewing the components with a conductive thread, and screen printing (Grabham et al., 2018). Conductive thread based MR coils (Vincent & Rispoli, 2020; D. S. Zhang & Rahmat-Samii, 2017) demonstrated the potential for wearable electro-textiles. These coils were created by sewing a conductive thread onto a non-conductive fabric. On the other hand, the conductive thread-based coils which were created this way; 1) had a quite short width, which was problematic in transmit mode, 2) were not durable and could be damaged easily, thus the coil might become open circuit, and 3) had a circuit hard to intervene such as adding or removing a component and changing the length of the coil.

This chapter introduced a single channel transceiver wearable elastic conductive textile (WECOT coil) ^{23}Na breast coil. WECOT coil was made from a 2-cm wide elastic textile produced by weaving a conductive thread along with an elastofiber. WECOT coil was wearable and able to stretch approximately twice more than its length at rest. A conventional transceiver ^{23}Na surface breast coil (SBC) having the same geometry as WECOT coil was also created for performance comparison. Bench measurements were carried out and phantom studies were performed to compare SNR performances of WECOT coil and SBC. A preliminary version of this work has been reported in (B. Kahraman-Agir, Bayrambas, B., Yegin, K., Ozturk-Isik, E., 2020).

3.2 Methods

3.2.1 Simulations and 3D Printing

Three breast phantoms, S-BP, M-BP, and L-BP, having prolate spheroidal structures with 627 mL, 785 mL, and 986 mL of volumes, respectively, were manufactured using 3D printing (Ultimaker2, Netherlands) (Fig. 3.1a). The volume and the size of the phantoms were 20% and 8% higher than the previous size, respectively. To simulate the performance of the coil, a T-belt surface 23Na breast coil (Fig. 3.1b) compatible with L-BP was created in 3D electromagnetic simulation software (Computer Simulation Technologies, CST, AG, Germany). The circumference of the top ring was 38 mm and the height of the coil was 81 mm. The material of the coil was chosen as Cu. The inductance of the coil was calculated at 32.6 MHz (the Larmor frequency of sodium at 3T). Three saline phantoms whose volumes were the same as S-BP, M-BP, and L-BP were created to load the coil. The conductivity of the phantom material was set to 2.8 S/m, which represented 300 mM of NaCl solution. Then, the coil was tuned on M-BP (Fig. 3.1d) with three serially connected capacitors (Fig. 3.2a). No further adjustments regarding the tuning were made when the coil was loaded with S-BP (Fig. 3.1c) and L-BP (Fig. 3.1e). Magnetic field density and B_1^- field (reception field) were calculated at z= 0 plane for each phantom.

3.2.2 WECOT Breast Coil

The elastic conductive textile was produced by weaving of a high-conductive silver thread (Statex, Germany) with elastofiber via full needle rib technique using a weaving machine (NSSG 122, Shima Seiki, Japan). The 2-cm wide elastic textile had 115% of elasticity when horizontally stretched. Two pieces of the textile with 14 cm and 12 cm lengths were cut to create the top ring of the T-belt geometry, whereas, a 10 cm of textile was used to create the bottom ring of T-belt geometry (Fig. 1c). The linear DC resistivity of the conductive thread was 30 Ω/m, whereas the AC resistance of WECOT coil was around 2.65 Ω.

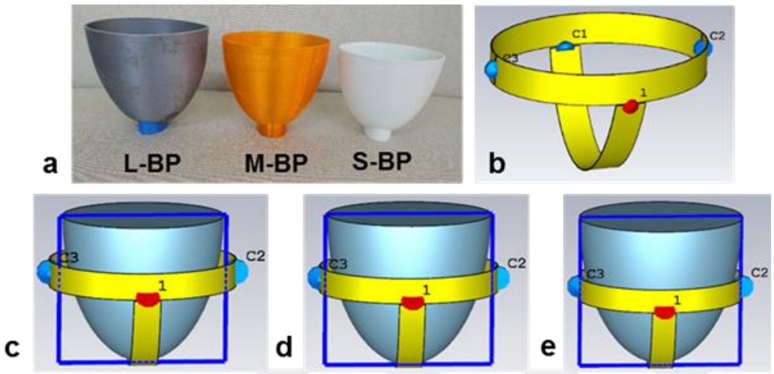

Figure 3.1 The prototypes. (a) Large (gray), medium (orange), and small (white) phantoms (Personal archive, 2021). (b) 3D model of the T-belt geometry, where C1, C2, and C3 were tuning capacitors and 1 represented the feed-port. S-BP (c), M-BP (d), and L-BP (e) placed inside the T-belt coil, respectively. Light blue solid in c, d, and e represented 300 mM of NaCl solution, whereas, blue rectangle was the slice at which B1- field was calculated

Because the conductive textile was silver coated polyamide, the circuit components could not be directly soldered on it. A connection circuit having 15 mm width and 20 mm length was designed on regular FR4 printed circuit board (PCB) (Fig. 2). Then, the capacitors were soldered on the connection circuit, and the conductive textile was sewn on both sides of the PCB through densely spaced plated-through-hole vias. Changes in linear resistance upon stretching were measured using a Multimeter (Rigol, DM3058) and a network analyzer (R&S ZVL13) at 32.6 MHz as displayed in Table 3.1.

The inductance of WECOT coil when it was on S-BP at 32.6 MHz was measured using a Network Analyzer (E5071C, Agilent Technologies, USA). The schematic representations of the coil and the matching circuit before the interface are illustrated in Fig. 3.3. WECOT coil was tuned by three capacitors, C_{T1}, C_{T2}, and C_{T3} when it was placed on L-BP (Fig. 3.2). No further adjustments related to tuning was made when WECOT coil wore S-BP and M-BP. The frequency shift occurred was 1.3 MHz and 2 MHz for M-BP and S-BP, respectively. The unloaded quality factor ($Q_{Unloaded}$) was calculated when each phantom was empty, whereas, the loaded quality factors were calculated when each phantom was filled with a 100 mM of NaCl solution (Q_{Sol100}) and a 300 mM of NaCl solution (Q_{Sol300}). All calculations were made at the -3dB level of |S11| (Mispelter, Lupu, & Briguet, 2006). Detuning and T/R switch was achieved by using a specially designed coil interface (Clinical MR Solutions, Brookfield, WI).

Table 3.1 Measured resistance of WECOT due to gradual increase of elasticity

Elasticity %	DC Resistance (Ω)	AC Resistance (Ω)
0	0.950 – 1.000	2.59
10	1.075 – 1.000	2.65
20	1.100 – 1.120	2.83
30	1.140 – 1.170	2.97
40	1.180 – 1.200	3.10
50	1.200 – 1.250	3.23

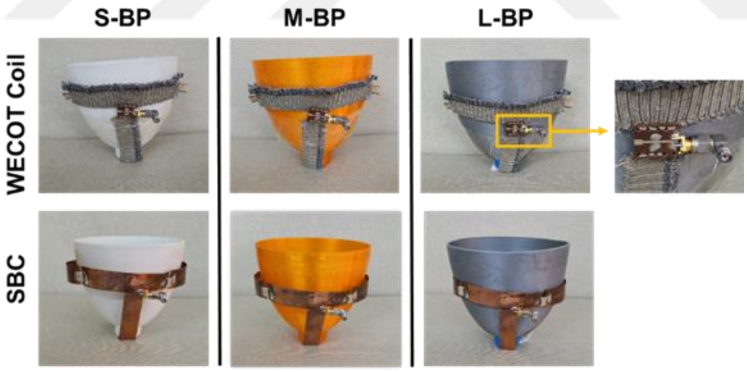

Figure 3.2 Loading of WECOT coil (top row) and SBC (bottom row) with S-BP, M-BP, and L-BP. Enlarged view of the connection circuit (demonstrated in yellow rectangle) was given next to WECOT coil wearing L-BP (Personal archive, 2021)

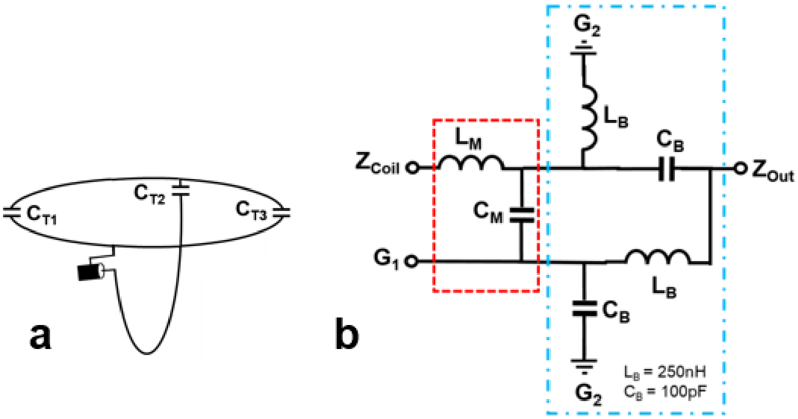

Figure 3.3 Circuit representation. (a) Location of the tuning capacitors on the coil, and (b) coil matching network and balun before the interface. The circuits in the red dotted and the blue dotted rectangles are the matching networks of the coil and the balun, respectively.

3.2.3 Conventional Surface Breast Coil (SBC)

Copper strip with 350 mm length and 20 mm width was cut to create the top ring, and a 170 mm long section was cut to create the bottom ring of the T-belt geometry (Fig. 3.2). The inductance of SBC at 32.6 MHz was measured using a Network Analyzer (E5071C, Agilent Technologies, USA). SBC was tuned on L-BP by three capacitors (Fig. 3.3a). Frequency shift occurred when SBC was loaded with S-BP and M-BP was negligible (0.1 MHz). $Q_{Unloaded}$ was calculated when SBC was empty. Similar to WECOT coil, the loaded quality factors were calculated when each phantom was filled with a 100 mM of NaCl solution (Q_{Sol100}) and a 300 mM of NaCl solution (Q_{Sol300}). All calculations were carried out at the -3dB level of |S11| . As before, detuning and T/R switch were accomplished by a specially designed coil interface (Clinical MR Solutions, Brookfield, WI).

3.2.4 Phantom Studies

Phantom studies were performed on a Siemens Magnetom Prisma 3T MRI scanner with multinuclear capability (Siemens Healthineers, Erlangen, Germany). Since the frequency shift occurred when WECOT coil was loaded with S-BP and M-BP cannot be compensated by the single-stage matching circuit, only phantom images of L-BP were acquired. Two different setups were used. In homogenous phantom setup, L-BP was filled with a 300 mM of NaCl solution (Sol_{300}) to obtain the reception profile of the breast coils. In multiple compartment setup (Fig. 3.4), L-BP was filled with a 100 mM of NaCl solution (Sol_{100}) along with a separate bottle of Sol_{300} to create an image contrast. Before sodium MRI acquisition of each setup, Proton MRI acquisition was performed via body coil, i.e. scanner's transmit and receive coil to adjust the shimming. WECOT coil and SBC were on L-BP during proton MRI acquisition.

T2 Turbo Spin Echo (TSE) sequence was applied for 1H imaging. Scan parameters were: TR/TE=6000/112 ms, flip angle=125°, voxel size = 0.47x0.47x4 mm, FOV= 240x240 mm, averages=2, Echo Train Length (ETL)=17 with a total scan time of 3:42 min. Both WECOT coil and SBC were used in transmit/receive mode. 80 V was applied to obtain a 90° flip angle. Fast low-angle shot (FLASH) sequence was applied for 23Na imaging. Scan paratemers were: TR/TE = 100/3.3 ms, flip angle= 90°, voxel size= 4x4x20 mm, FOV= 320x320 mm, averages= 32 with a total scan time of 4:15 min. Short echo time was determined due to low signal intensity of sodium and for SNR consideration.

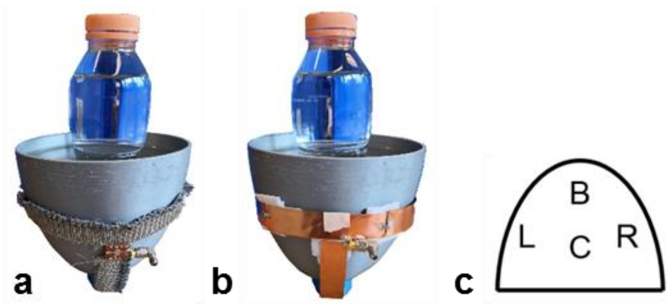

Figure 3.4 Multiple compartment setup: (a) WECOT coil, (b) SBC and (c) selected regions of the phantom for calculation of SNR. B, L, R, and C represent the bottom, the left-hand side, the right-hand side, and the center of the phantom, respectively (Personal archive, 2019)

3.3 Results

3.3.1 Simulation

The simulated inductance and the value of each tuning capacitor of the T-belt breast coil were 117 nH and 320 pF, respectively. Simulated magnetic field intensity (*H*) of the phantoms was similar to each other in terms of an increase in B, L, and R, and a decrease towards the center of each phantom (Fig. 3.5), such that it was between 80-150 A/m in B, 60-80 A/m in L and R, and 20-40 A/m in C. However, a gradual decrease in H from S-BP to L-BP was noticeable. Simulated B_1^- field (Fig. 3.5) correlated with the simulated magnetic field intensities in terms of the field distribution throughout the phantoms. The high intensity of B_1^- field calculated on the surface of the phantoms around the coil was discernible.

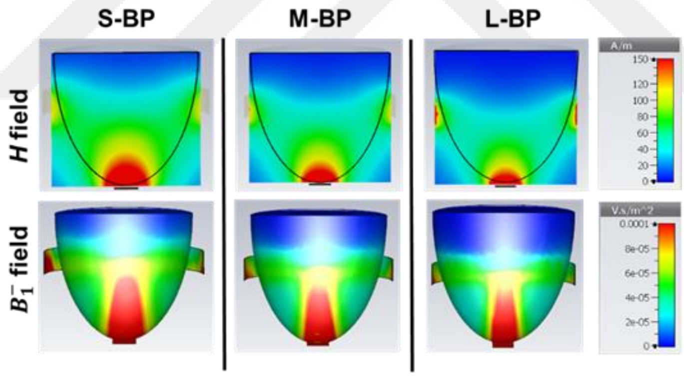

Figure 3.5 Simulated distributions of magnetic field intensity (H) (top row) and (c) B_1^- field (bottom row) of the T-belt breast coil for each phantom (Personal archive, 2021)

3.3.2 Bench Measurements

Measured inductances of SBC and WECOT coil when it was on empty L-BP were 131 nH and 125 nH, respectively. With C_{T1}= C_{T3}, C_{T1}, C_{T2}, L_M, and C_M of WECOT coil were 220pF (ATC Corp., USA), 270pF (ATC Corp., USA), 39 nH (0603HP, CoilCraft Inc., USA), and 390 pF (S111DUE, Johanson Technology Inc., USA), respectively. With C_{T1}= C_{T3}, C_{T1}, C_{T2}, L_M, and C_M of SBC were 270pF, 220pF, 12 nH, and ~850 pF (560pF//270pF//20pF), respectively. DC conductivity of Sol_{100} and Sol_{300} was 0.94 S/m and 2.87 S/m (Inolab Cond 720, WTW). The increase in $Q_{Unloaded}$ of WECOT coil was proportional to the increase in size of the phantoms (Fig. 3.6a). $Q_{Unloaded}$ of SBC was 326 (Fig. 3.6b). Q_{Sol100} and Q_{Sol300} values of WECOT coil for S-BP, M-BP, L-BP were 41, 43, 46, and 30, 28, 30, respectively (Fig. 3.6c). Q_{Sol100} and Q_{Sol300} values of SBC for S-BP, M-BP, and L-BP were 256, 218, 204 and 172, 148, 109, respectively (Fig. 3.6d). The corresponding Q_{Ratio} of Sol_{300} was approximately 1.5 times that of Sol_{100} in both WECOT coil and SBC. According to loss tangent (σ/ωε ratio), the solution behaves like a quasi-conductor and the attenuation is proportional to the square root of the conductivity (Ulaby, Michielssen, & Ravaioli, 2015), which correlates well with the Q_{Ratio}. |S11| of WECOT coil and SBC when they were matched on L-BP, were -12.5 dB and -12 dB, respectively.

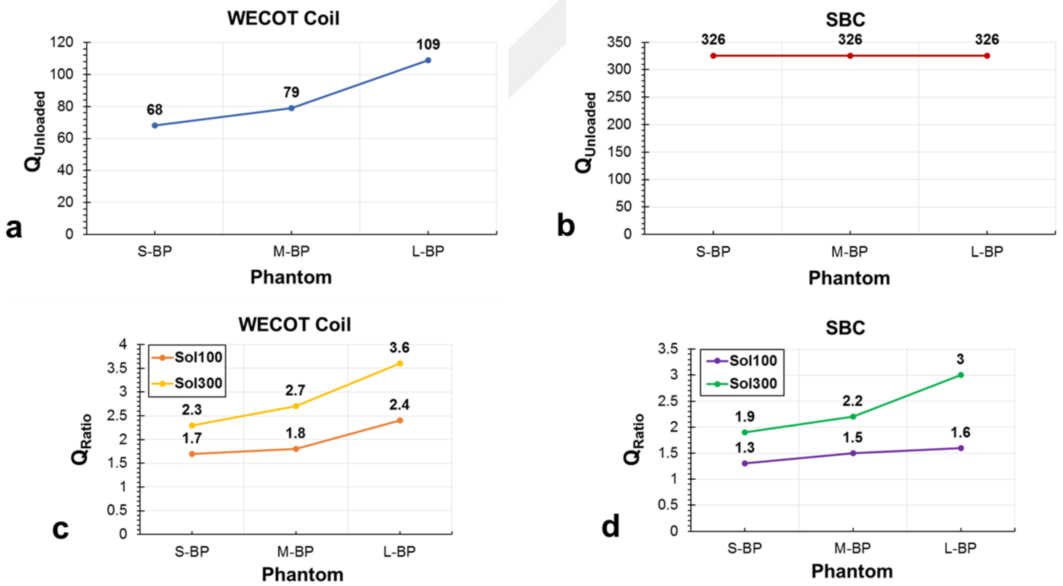

Figure 3.6 $Q_{Unloaded}$ values of (a) WECOT coil and (b) SBC according to the phantom of interest. Q_{Ratio} values of (c) WECOT coil and (d) SBC when they were loaded with Sol_{100} and Sol_{300}

3.3.3 Phantom Studies

Proton MR image and SNR distribution of the multiple compartment setup when WECOT coil was on L-BP are shown in Figs. 4.7a and 4.7b. Although this image was acquired for shimming purposes, L-BP filled with Sol_{100} and a separate bottle containing Sol_{300} were clearly distinguishable. PCB connection circuits with very low resistance and no B_1 return appeared as dark spots on the image as expected.

^{23}Na MR images of both coils in homogenous phantom setup (Fig. 3.7c,g) were similar in terms of their ability of signal transmission and reception. Calculated SNR was quite high in regions near the coil compared to the center of the phantom, such that it was varying from 80 to 140 in B, from 50 to110 in L and R, and from 20 to 50 in C (Fig. 3.7e ,i). SNR of WECOT coil was evidently better at L and R, but limited at C.

In multiple compartment setup, SNR was between 60-140 in B, 20-40 in L, R, and C (Fig. 3.7f,j). The contrast between Sol_{300} and Sol_{100} was noticeable in B (Fig. 3.7d,h). SNR of L and R in Fig. 3.7f,j decreased compared to that of L and R in Fig. 3.7e,i in accordance with the decrease in the concentration of the loading. Yet, the concentration difference was not distinguishable in C. The SNR ratios of Sol_{300} to Sol_{100} sections measured with the WECOT coil and SBC were 4.17 and 2.92, respectively (Fig. 3.8). Reduced ability of WECOT coil to transmit/receive a signal from C was also observed in Fig. 3.7d,f.

To compensate for the inhomogeneous magnetic field, reception profiles acquired from the homogenous phantom setup were used to correct the multiple compartment setup images (Fig. 3.9). Gaussian and median filters were applied to the sensitivity maps. Sensitivity maps were used to scale the images of the multiple compartment setup to obtain better contrast images.

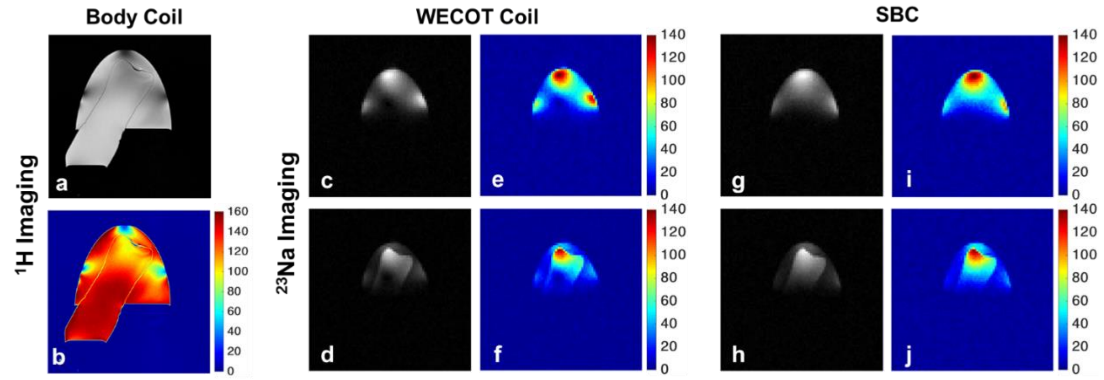

Figure 3.7 Phantom MR images of the body coil (left), WECOT coil (middle), and SBC (right). (a) ^{1}H image of multiple compartment setup and (b) its SNR map. (c,g) ^{23}Na images of homogenous phantom setup and (e,i) their SNR maps, respectively. (d,h) ^{23}Na images of multiple compartment setup and (f,j) their SNR maps, respectively

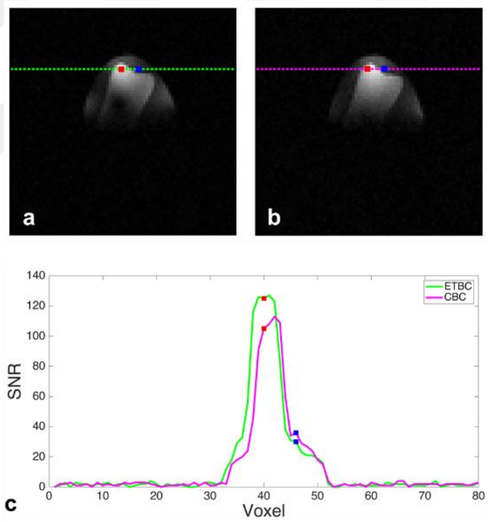

Figure 3.8 The lines chosen to compare SNR of Sol_{300} (red marker) and Sol_{100} (blue marker) of (a) WECOT coil and (b) SBC, and (c) their corresponding SNR profiles

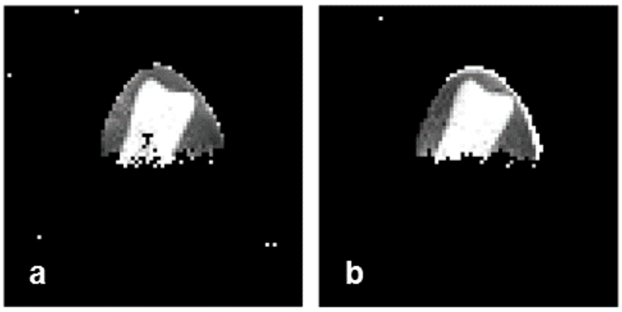

Figure 3.9 Multiple compartment setup images of (a) WECOT coil and (b) SBC corrected by the reception profiles shown in Fig. 3.7d and Fig. 3.7h, respectively

3.4 Conclusion

In this work, the formation of conductive textile with elastofiber using a weaving machine has provided considerable benefits in obtaining a conductive textile strip with desired percentage of elasticity and width. The textile could then be cut into desired pieces to create a coil as in the case of creating a conventional coil using copper strips. Custom-made connection circuits were easy to sew, to solder on it, and to unstitch, if necessary. Moreover, the elastic feature of WECOT coil enabled flexibility in determining the target volume, adjustability with the phantom, and also provided a better loading factor. Indeed, minimal change observed in $Q_{Unloaded}$ values and Q_{Loaded} values almost remained the same regardless of the size of the phantom. Loading a coil increases the inductive reactance and thus causes a shift at the resonance frequency. On the other hand, the wavelength was approximately 9 m at 32.6 MHz, which in turn, minimized the frequency shift resulting from different loadings, such as Sol_{100} and Sol_{300}. However, higher concentration of Sol_{300} provided more loading than Sol_{100}, which was verified by $Q_{100ratio}$ and $Q_{300ratio}$ (Fig. 3.6) of both WECOT coil and SBC. In addition, the high linear resistivity of WECOT coil resulted in lower Q compared to those of SBC.

Measured inductance and tuning capacitance of WECOT coil corroborated with those of simulation results. In addition, simulated H field and B_1^- field had similar distributions to Fig. 3.7e in terms of signal transmission and signal reception. This also indicated that the textile coils could be modeled as Cu coils to study field distributions in electromagnetic simulation programs.

Extracellular sodium concentration (ESC) in human body is 150 mM (Madelin et al., 2014). The concentration of solution in homogenous phantom setup was determined as Sol_{300} which was particularly higher than ESC to receive higher signal for a realistic reception profile. Sol_{100} which was lower than ESC was determined to demonstrate that WECOT coil and SBC could operate in 100-300 mM range. The distance of the bottom, the left-hand side, and the right-hand side border to the coil was minimum and that of the center was maximum. Accordingly, since the magnetic field strength decreases away from the current source, it was expected that SNR of the bottom, the left-hand side, and the right-hand side of the border was higher than the center. The calculations in Fig. 3.8 were performed to verify whether the coils provided correct information depending on the concentration of the solutions or the bottom region was the oversensitive area just because of its proximity to the coil. Red marker to blue marker ratio was expected to be approximately 3 since the Sol_{300} to Sol_{100} ratio was 3. Considering that these ratios were 4.17 and 2.92 (Fig. 3.8) for WECOT coil and SBC, respectively, one may infer that the bottom region of Fig. 3.7b yielded a correct estimate, whereas the bottom region of Fig. 3.7a was a little oversensitive, although it had higher SNR than that of Fig. 3.7b. Furthermore, the decrease in SNR of the left-hand side and the right-hand side of the border of Fig. 3.7f,j compared to that of Fig. 3.7c,g indicated that WECOT coil and SBC were functioning accurately in these regions as well.

Considering the resistivity of the conductor is one of the primary noise sources in MRI, it is expected that SNR of MR images acquired by WECOT coil would be lower than those of the SBC. WECOT coil was able to stretch horizontally and retract in accordance with the phantom in use, yet the increase in resistance (Table 3.1) unavoidably caused coil noise. Electronically tuned broad-band matching circuit to accommodate even larger shifts in resonance can be designed in future studies. Besides breast imaging, WECOT coil can also be used for body parts which require greater flexibility such as hand, foot, wrist, ankle, elbow, and knee.

This study had some limitations. Since MRI systems generally do not have the sodium transmit ability through the body coil, designed sodium coils have to enable signal transmission as well (Bangerter, Kaggie, Taylor, & Hadley, 2016). The preferred geometry for signal transmission is usually different than the one used for reception. Basically, large coils are suitable for the signal transmission due to their large field of view (FOV). On the other hand, small coil elements, such as coil arrays, are preferred for signal reception due to their small B_1^- profile. Employing the same geometry for both transmission and reception inevitably results in an SNR penalty owing to these conflicting goals and due to the fact that the capability of receiving signal from the region of interest (ROI) is limited by the excitation profile. Designing a large textile coil would hardly satisfy the wearable condition of the coil, and also, the interface used for ^{23}Na MRI had only one input. Thus, the WECOT coil was primarily designed as a surface coil. Although the T-belt geometry created the magnetic field in coronal and sagittal planes, it still needed further refinement to produce a homogeneous magnetic field in the entire ROI, which is a common problem for all surface coils. Moreover, obtained reception profiles represented the inhomogeneous excitation profiles of the coils.

CHAPTER 4

FOUR-CH BILATERAL ^{1}H WECOT BREAST COIL

4.1 Introduction

The worldwide prevalence of breast cancer and its predominance on cancer mortality highlight the importance of early diagnosis to increase the survival rate. Magnetic resonance imaging (MRI) is preferred as an adjunctive method to increase the sensitivity and the specificity of the diagnosis. Unlike mammography and ultrasound, MRI provides pathophysiological information of the suspicious lesions by contrast enhancement (Heywang-Kobrunner et al., 2013). In addition, clinical breast diffusion weighted imaging (DWI) and three-time point (3TP) studies has proven to distinguish malignant and benign tumors (Jacobs et al., 2004). A dedicated breast radiofrequency (RF) coil could improve the evaluation of MR imaging techniques and signal-to-noise-ratio (SNR).

In conventional breast RF coil designs, hemispherical (By et al., 2014; Kaggie et al., 2014; Nnewihe et al., 2011) or cylindrical (Brown et al., 2014; McDougall et al., 2014) structures with a predetermined target volume are employed. Yet, although the breast anatomy is similar in healthy women, the breast size can vary regardless of age and weight. In case of the incompatibility between the breast coil in use and the patient's breast size, the predetermined target volume of a coil may lead to the alteration of the loading factor, and hence the resonance frequency. The shifted resonance frequency can deteriorate the reflection coefficient; therefore, SNR of the resultant image may decrease. Moreover, when larger breasts are squeezed in the coil housing, not only the time-signal intensity curve shapes are affected, but higher signal intensities where the breast is touching the coil may occur or a pushed down nipple into the breast parenchyma can prevent the nipple enhancement (Ojeda-Fournier et al., 2007). Besides SNR penalty and the prevention of a proper diagnosis, the coil diameter limiting the depth of magnetic field penetration affects the reception or the transmission profile. Considering all these issues, a size adjustable coil would provide significant improvements.

Introduced screen printed (Corea et al., 2016; Hancu et al., 2016; Winkler et al., 2019) and flexible (Frass-Kriegl et al., 2018; Vasanawala, 2017) RF coil arrays have demonstrated bendable and conformal features; however, in actual fact, they have had fixed target volumes. An inflexible copper (Cu) coil whose target volume could be adaptable in accordance with the different sized phantoms has been presented (B. Zhang et al., 2019). Recently, wearable detector arrays composed of liquid metal (Port et al., 2020), coaxial cable (B. Zhang et al., 2018), and Cu braid (Nordmeyer-Massner et al., 2012) have been studied.

Conductive textiles have been utilized in the form of Cu wire coated with silk or polyamide, sewing the components with a conductive thread, and screen printing by means of the recent advances in on-body communications and sensors (Grabham et al., 2018). RF coils made by sewing a conductive thread onto a non-conductive fabric (Vincent & Rispoli, 2020; D. S. Zhang & Rahmat-Samii, 2017) are promising applications of wearable electro-textiles in MRI. On the other hand, there were three major drawbacks of conductive-thread based coils which were produced by sewing. Firstly, the short width of the coil, which was usually limited by the sewing operation and the width of the conductive thread itself, might lead to problems in transmit mode. Secondly, having short width ran a risk of the coil becoming open circuit in case of a circuit damage. Thirdly, the intervention to the coil circuit, for instance adding or removing a component was quite troublesome.

Previous studies (B. Kahraman-Agir, Bayrambas, B., Yegin, K., Ozturk-Isik, E., 2019, 2020; B. Kahraman-Agir, Yegin, & Ozturk-Isik, 2021) had validated the applicability of the elastic conductive textiles in MR engineering. The goal of this study was to demonstrate a multichannel application of elastic conductive textile on different sized phantoms and proton breast MRI. The subsequent goal was to achieve minimum 0.5 mm of resolution in MR images to be acquired. Firstly, a two-channel lateral wearable elastic conductive textile (WECOT) breast coil (BC) was introduced including the production of elastic conductive textile, the design of WECOT-BC, the solutions related to the circuitry, and the broadband matching. Secondly, a two-channel lateral conventional Cu breast coil was created for comparison. Finally, a four-channel bilateral WECOT-BC was presented. SNR and resolution performance of all coils were tested via phantom studies.

4.2 Methods

4.2.1 3D Printing and Simulations

Three breast phantoms, S-BP (627 mL), M-BP (785mL), and L-BP (986 mL) whose volumes and dimensions were progressively 20% and 8% higher than the previous size, respectively were designed in a 3D Computer Aided Design (CAD) software (ThinkDesign, DPT Corporate, Italy). The volume of S-BP was determined considering the average breast volume of women is approximately 650 mL (McGhee & Steele, 2011). The phantoms had prolate spheroidal structure to represent released breasts inside a coil during an MR scan. Correspondingly, three single channel saddle breast coils, S saddle coil, M saddle coil, and L saddle coil, compatible with S-BP, M-BP, and L-BP, respectively, were created in 3D electromagnetic simulation software (Computer Simulation Technologies, CST, AG, Germany) to simulate WECOT breast coil (Fig. 4.1a). The material of the coils was chosen as Cu. The inductances of the coils were calculated at 123.2 MHz (the Larmor frequency of proton at 3 T). M saddle coil was tuned with a tuning capacitor, C_T. Then, the capacitance of C_T was assigned to that of S saddle coil and L saddle coil. No further adjustments related to the tuning was made. The impedances of S saddle coil and L saddle coil were recorded. The frequency shift (Δf) on S saddle coil and L saddle coil resulting from the change in impedance was given in Table 4.1. Afterwards, S-BP, M-BP, and L-BP were printed in a 3D printer (Ultimaker2, Netherlands).

To simulate CBC, two-channel L-sized crosswise saddle breast coil (Fig. 4.1b) created in CST. Three saline phantoms, S saline phantom, M saline phantom, and L saline phantom, having the same volume as S-BP, M-BP, and L-BP were also designed in CST. The conductivity of the saline solution was determined as 0.5 S/m, representing benign breast tissue (Shin et al., 2015). The coil was tuned with three serially connected capacitors while it was loaded with M-saline phantom. The angle between the crosswise rings (Fig. 4.2a) enabling the best decoupling was 84°. No further adjustments regarding the tuning was made when the coil was loaded with S saline phantom and L saline phantom. The frequency shift occurred when the coil was loaded with different saline phantoms (S and L) was recorded. *H* field (magnetic field intensity) and B_1^- (reception field) were calculated at x= +35 and y= +70 planes when the coil was loaded with S, M, and L saline phantom, respectively.

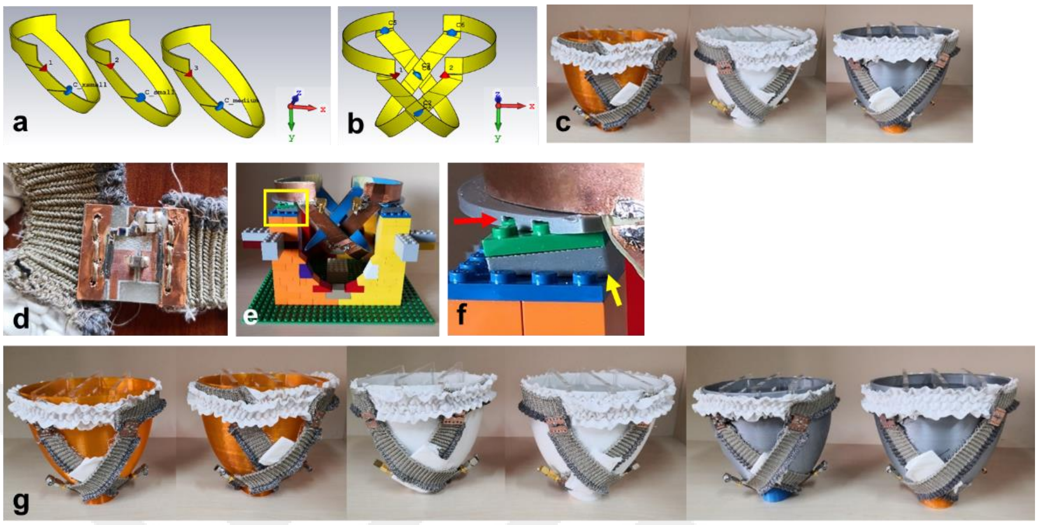

Figure 4.1 (a) CST simulations of S, M, and L saddle coil. (b) CST simulation of two-ch CBC. (c) two-ch lateral WECOT-BC on S (orange), M (white), and L (gray) phantoms (Personal archive, 2020). (d) The detuning circuit of on the connection circuit (Personal archive, 2020). (e) Two-ch lateral CBC built on blue scaffolds (Personal archive, 2020). (f) Enlarged view of the yellow frame in (e) demonstrating the scaffold (red arrow) compatible with the building blocks and the custom-made 5° inclined building block (yellow arrow) (Personal archive, 2020). (g) Four-ch bilateral WECOT-BC wearing S (orange), M (white), and L (gray) phantoms (Personal archive, 2020)

Table 4.1 The simulated inductance, impedance, and frequency shift of S, M, and L saddle coils when they were on their corresponding saline phantoms

Coil	**L (nH)**	**C_T (pF)**	**Z (Ω)**	**Δf**
S saddle	196	7.5	0.1-j13	6
M saddle	249	7.5	0.5+j0.1	Center
L saddle	309	7.5	0.2+j20	8

4.2.2 Two-ch Lateral WECOT-BC

A high-conductive silver thread (Statex, Germany) whose linear resistivity was 30 Ω/m, was woven with an elastofiber in a weaving machine (NSSG 122, Shima Seiki, Japan) via full needle rib technique to create an elastic conductive textile. The resultant 2-cm wide textile had 115% of elasticity when horizontally stretched. The proposed CU saddle structure consisted of a C shaped WECOT placed on the top of the phantom and a U shaped WECOT positioned diagonally to the bottom of the phantom. Three pieces of textile, such that 80 mm of textile composed C part, whereas, 80 mm and 100 mm of textile created U part of each channel of WECOT-BC. The channels were prevented from touching each other by means of a piece of napkin (Fig. 4.1c). The DC resistance of two channels were 3.4 Ω and 3.3 Ω, respectively.

Because the conductive thread contained polyamide, the circuit components cannot be directly soldered on WECOT. Thus, custom-made 15 mm-wide and 20 mm-long printed-circuit-board (PCB) connection circuits were designed (Fig. 4.1d). Afterwards, three connection circuits were sewn on each channel of WECOT-BC.

The inductance of each channel of WECOT-BC at 123.2 MHz (the Larmor frequency of proton at 3T) was measured using a Network Analyzer (ZVL, Rohde&Schwarz, Germany). A NaCl-$CuSO_4$ solution (2.5 g of NaCl, 0.5 g of $CuSO_4.5H_2O$, 1 L of deionized water) was used to load the phantoms during the tuning. Channel 1 (Ch1) was tuned on M-BP by two C_T (Fig. 4.2b). $Z_{WECOTCh1}$ and $Z_{WECOTch2}$ in Figure 5.2b were the impedance of Ch1 and Channel 2 (Ch2), respectively. The impedance and the frequency shift occurred when it was on S-BP, M-BP, and L-BP were recorded. The angle between U parts providing the decoupling, α, (Fig. 4.2a) was adjusted experimentally. Detuning was achieved by 27 nH (0603HP, CoilCraft Inc., USA) and two pin diodes (MA4P1250NM -1072T, Macom, USA) (Fig. 2b). These steps were repeated for Ch2. The measured inductances of Ch2 of WECOT-BC when it was placed on empty S-BP, M-BP, and L-BP were 300 nH, 365 nH, and 470 nH, respectively. A three-stage matching circuit (Fig. 4.2e) was designed to compensate Δf and maintain the matching for three phantoms. Inductors (0603HP, CoilCraft Inc., USA), variable capacitors (Passive Plus Inc., USA), and fixed capacitors (Johansson

Technology, USA) were used in the tuning and the matching. L1, C1, L2, C2, L3, C3 values of Ch1 were 22nH, 130-160pF tuneable, 47nH, 60-80pF tuneable, 100nH, 30-40pF tuneable, respectively and L1, C1, L2, C2, L3, C3 values of Ch2 were 22nH, 130-160pF tuneable, 47nH, 60-80pF tuneable, 100nH, 30-40pF tuneable, respectively. An RF transformer was used as balun (ADT 1-1+, Mini-Circuits, USA). The unloaded ($Q_{Unloaded}$) and loaded (Q_{Loaded}) quality factor were calculated when the coil was on S-BP, M-BP, and L-BP. All calculations were made at the -3dB level of the reflection coefficient (Mispelter et al., 2006).

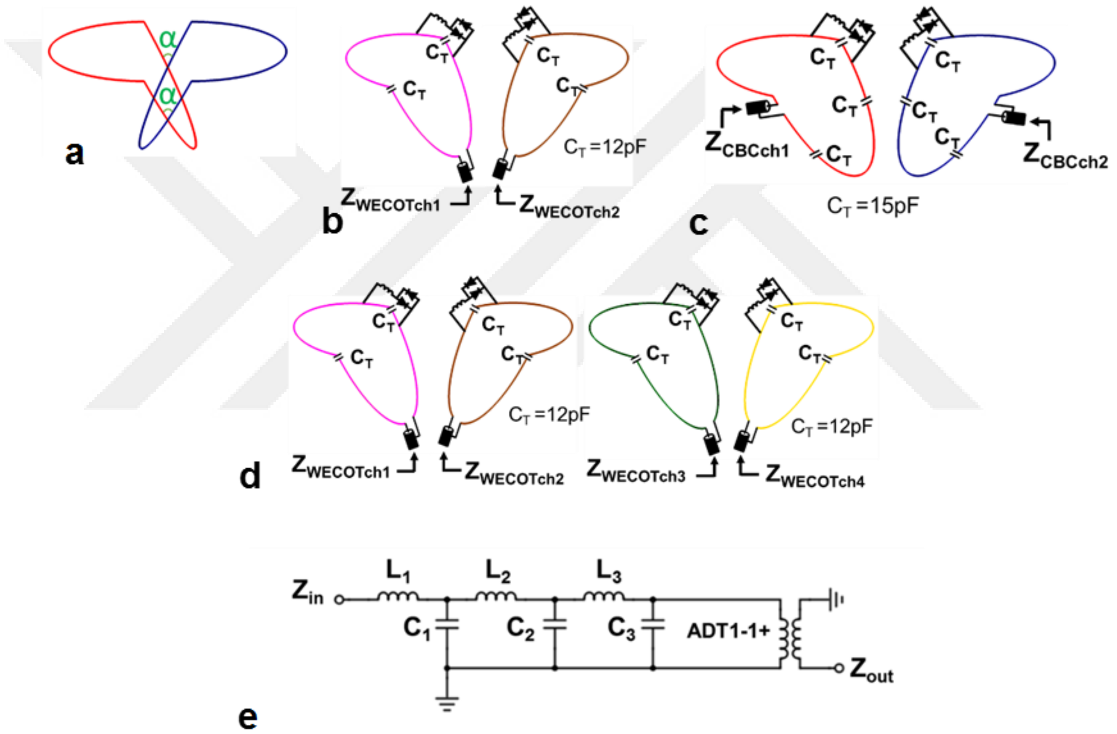

Figure 4.2 The circuit schematics. (a) The placements of the crosswise saddle structure, where α is the overlap angle. (b) Two-ch lateral WECOT-BC. (c) Two-ch lateral CBC. (d) Four-ch bilateral WECOT-BC. (e) Three-stage matching circuit where each LC pair indicates a stage

4.2.3 Two-ch Lateral Conventional Breast Coil (CBC)

Two CU shaped scaffolds closely fitting L-BP were modelled in a 3D Computer Aided Design (CAD) software (ThinkDesign , DPT Corporate, Italy). Since CBC was planned to stand on a stillage made from building blocks (Lego, Lego Group, Billund, Denmark), the scaffolds were designed to fit the surface of the building blocks (Fig. 4.1f). The scaffolds were printed in a 3D printer (Ultimaker2+, NL) with a polylactic acid (PLA) printing material. Afterwards, they were covered with a 20 mm-wide and 6 mm-thick copper strip (Fig. 4.1e). NaCl-$CuSO_4$ solution (2.5 g of NaCl, 0.5 g of $CuSO_4.5H_2O$, 1 L of deionized water) was used to load the phantoms during the tuning. Each channel was tuned by three serially connected capacitors, C_T, (Fig. 4.2c) when the coil was loaded with M-BP. The impedance of channels, which were demonstrated as Z_{CBCCh1} and Z_{CBCch2} in Fig. 4.2c, measured on each phantom and the frequency shift occurred when the coil was on S-BP and L-BP was recorded. α (Fig. 4.2a) was adjusted to yield a good decoupling by two custom-made 5° inclined building blocks for each channel (Fig. 4.1f). Detuning was achieved by 33 nH of inductor (0603HP, CoilCraft Inc., USA) and two pin diodes (MA4P1250NM -1072T, Macom, MA, USA). 2-stage impedance matching circuit (Fig. 4.2e) was designed to sustain the matching for three phantoms. Inductors (0603HP, CoilCraft Inc., USA), variable capacitors (Passive Plus Inc., USA), and fixed capacitors (S11DUE, Johansson Technology, USA) were used. L1, C1, L2, C2 values of Channel 1 were 47nH, 56pF, 47nH, 68pF, respectively and L1, C1, L2, C2 values of Channel 2 were 47nH, 82pF, 47nH, 47pF, respectively. An RF transformer was used as balun (ADT 1-1+, Mini-Circuits, NY, USA). $Q_{Unloaded}$ and Q_{Loaded} were calculated when the coil was on S-BP, M-BP, and L-BP. All calculations were made at the -3dB level of the reflection coefficient (Mispelter et al., 2006).

4.2.4 4-ch Bilateral WECOT-BC

Channels of two-ch lateral WECOT-BC were used as first and second channel of 4-ch bilateral WECOT-BC (Fig. 4.1g). The methods of two-ch lateral WECOT-BC was repeated to create third (Ch3) and fourth (Ch4) channel of bilateral WECOT-BC (Fig. 4.2d). DC resistance of Ch3 and Ch4 was 3.3 Ω and 3.2 Ω, respectively. The measured inductances of Ch3 of WECOT-BC when it was placed on empty S-BP, M-BP, and L-BP were 325 nH, 375 nH, and 500 nH, respectively The frequency shift occurred when the coil was on S-BP and L-BP was recorded. Detuning was achieved by 27 nH (0603HP, CoilCraft Inc., USA) and two pin diodes (MA4P1250NM -1072T, Macom, MA, USA). Three-stage impedance matching circuit (Fig. 4.2e) was designed to remain the matching for three phantoms. L1, C1, L2, C2, L3, C3 values of Ch3 were 22nH, 130-160pF tuneable, 47nH, 60-80pF tuneable, 100nH, 30-40pF tuneable, respectively and L1, C1, L2, C2, L3, C3 values of Channel 4 were 22nH, 130-160pF tuneable, 47nH, 60-80pF tuneable, 100nH, 30-40pF tuneable, respectively. An RF transformer was used as balun (ADT 1-1+, Mini-Circuits, NY, USA). The loaded quality factor (Q_{Loaded}) was calculated when the coil was on S-BP, M-BP, and L-BP. All calculations were made at the -3dB level of the reflection coefficient (Mispelter et al., 2006).

4.2.5 Phantom Studies

Phantoms were filled with NaCl-$CuSO_4$ solution (2.5 g of NaCl, 0.5 g of $CuSO_4.5H_2O$, 1 L of deionized water) to adjust the conductivity of the solution to 0.5 S/m (Shin et al., 2015). The conductivity was measured as 0.56 S/m (DAK12 Dielectric Probe, Agilent, USA) at 123.2 MHz. A resolution plate having three sagittal (S1, S2, S3) and two coronal (C1,C2) components (Fig. 4.3a) which can intertwine each other (Fig. 4.3c) was designed in a 3D CAD software (ThinkDesign , DPT Corporate, Italy). Four individual holes and a pattern of four elements were modelled on each component (Fig. 4.3b). Each element of the pattern was composed of lines and holes. The thickness of the lines and the diameter of the holes varied from 0.25 mm to 2 mm. Diameter of four individual holes varied from 2 mm to 6 mm. The resolution plate was produced by a Laser engraving and cutting machine (Bodor Laser).

Phantom studies were performed on a Siemens Magnetom Trio 3T MRI scanner (Siemens Healthineers, Erlangen, Germany). Phantom images of two-ch lateral WECOT-BC, two-ch lateral CBC, and 4-ch bilateral WECOT-BC were acquired. Each coil was tested on S-BP, M-BP, and L-BP. A slice in sagittal plane and a slice in coronal plane were acquired for each phantom when the resolution plate was placed (Fig. 4.3d). Then, the resolution plate was removed to acquire the reception profile of the coil in the same slices. MR images of the phantom with the resolution plate were corrected using the corresponding reception profile. Gradient Echo (GRE) sequence was applied for proton MRI. Scan parameters when two-ch coils were tested were: FOV=150 x 150 mm, voxel size= 0.5 x 0.5 x 5 mm, TR/TE= 100/4.8 ms. Scan parameters when 4-ch WECOT coil was tested were FOV=330 x 330 mm, voxel size= 1.2 x 1.2 x 5 mm, TR/TE= 100/4.8 ms.

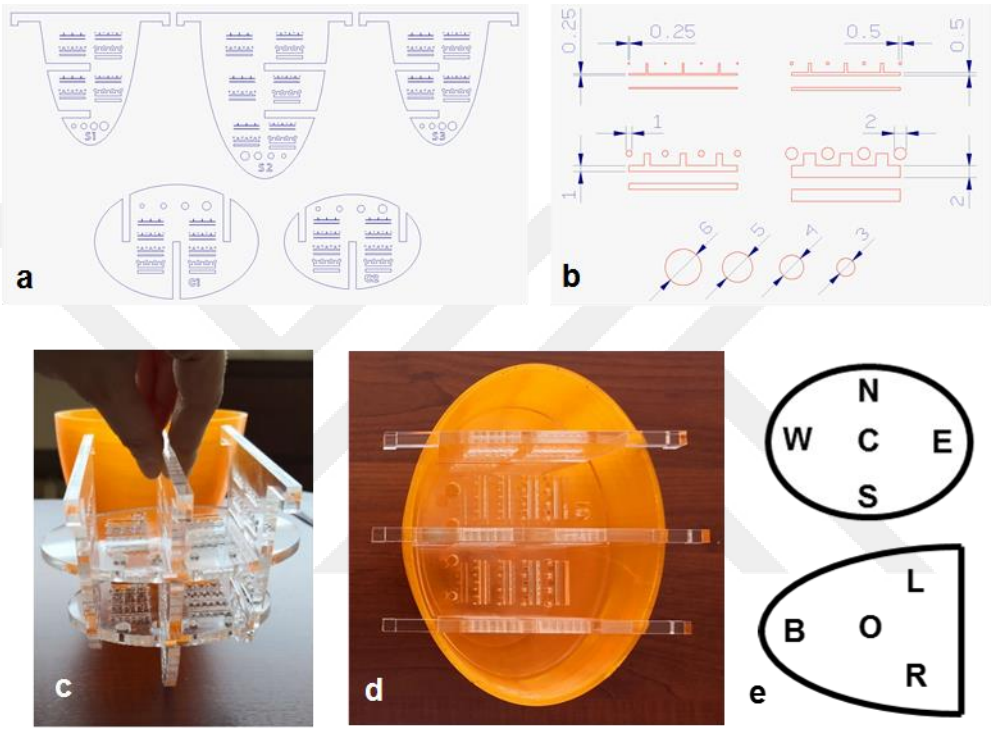

Figure 4.3 (a) Three sagittal plates (top), two coronal plates (bottom) of the resolution plate. (b) Dimensions of the pattern on the resolution plate. (c) Sagittal plates and coronal plates intertwined each other (Personal archive, 2020). (d) The resolution plate placed inside S-BP (Personal archive, 2020). (e) Selected regions for SNR interpretations of coronal (top) and sagittal (bottom) slices. While E, W, N, S, and C refer to eastern, western, northern, souther, and center part of the phantom, B, O, L, and R stand for the bottom, the center, the left-hand side, and the right-hand side of the sagittal slice

4.3 Results

4.3.1 Bench Measurements

4.3.1.1 Two-ch Lateral WECOT-BC

The change in reactance, ΔXL, when Ch1 was on S-BP and L-BP was 15 Ω and 14 Ω, respectively in Table 4.2. The corresponding change in inductance, ΔL, was 19.4 nH and 18.1 nH, respectively. ΔX_L of Ch2 was 10 Ω and 16 Ω for S-BP and L-BP, respectively. The corresponding change in inductance, ΔL, was 12.9 nH and 20.7 nH, respectively. In addition, the increase in resistivity of the coil was proportional to size of the phantom.

8 MHz and 7 MHz of frequency shift occurred when the coil wore S-BP and L-BP, respectively. |S11| values when WECOT-BC wore S-BP, M-BP, and L-BP were -12 dB, -11.5 dB, and -9.6 dB, respectively. |S22| values when the coil was loaded with S-BP, M-BP, and L-BP were -11 dB, -27 dB, and -11 dB, respectively. |S21| values when the coil was on S-BP, M-BP, and L-BP were -16 dB, -26 dB, and -42 dB, respectively. $Q_{Unloaded}$ values (Fig. 4.4) of WECOT-BC was increased gradually as the size of the phantom increased. However, numerical values of Q_{Loaded} did not demonstrate a dramatic change by remaining in 80-100 range for all phantoms. Accordingly, Q_{Ratio} values (Fig. 4.4) demonstrated incremental change as the size of the phantom increased.

4.3.1.2 Two-ch Lateral CBC

1 Ω of reactance change was observed in both channels when they were loaded with S-BP and L-BP (Table 4.2). The corresponding ΔL was 1.3 nH. It was similar to the case in WECOT coil that CBC’s resistivity increased as the size of the phantom increases. On the other hand, the nominal value of its resistivity was lower than that of WECOT coil. |S11| values when the coil was loaded with S-BP, M-BP, and L-BP

phantom were -14 dB, -15 dB, and -17 dB, respectively. |S22| values when the coil wore S-BP, M-BP, and L-BP were -17.5 dB, -16.5 dB, and -14 dB, respectively. |S21| values when the coil was on S-BP, M-BP, and L-BP were -15 dB, -15.5 dB, and -16 dB, respectively. Q_{Ratio} values (Fig. 4.4) increased as the size of the phantom, and therefore the loading increased, which is a typical behaviour of a copper coil. In addition, Ch2 yielded higher Q_{Ratio} than Ch1.

4.3.1.3 4-ch Bilateral WECOT-BC

ΔX_L of Ch3 for S-BP and L-BP was 10 Ω and 16 Ω, respectively in Table 4.2. The corresponding change in inductance, ΔL, was 12.9 nH and 20.7 nH, respectively. ΔX_L of Ch4 for S-BP and L-BP was 11 Ω and 18 Ω, respectively. The corresponding change in inductance, ΔL, was 14.2 nH and 23.3 nH, respectively.

The frequency shift occurred when the coil was on S-BP and L-BP was 8 MHz and 7 MHz, respectively.|S33| values when the coil wore S-BP, M-BP, and L-BP were -15 dB, -13 dB, and -8 dB, respectively. |S44| values when the coil was on S-BP, M-BP, and L-BP were -12 dB, -20.5 dB, and -8.7 dB, respectively. |S43| values when the coil was loaded with S-BP, M-BP, and L-BP were -23 dB, -30 dB, and -28 dB, respectively. Similar increase in $Q_{Unloaded}$ and Q_{Ratio} values as in Ch1 and Ch2 were observed in Ch3 and Ch4 (Fig. 4.4) and it was in accordance with the increase in the loading. Additionally, numerical values of Q_{Loaded} on different phantoms stayed in 80-115 range as in Ch1 and Ch2.

4.3.2 Reception Profiles

Figure 4.5 shows the reception profiles of the coils obtained after the resolution plate was removed in the same scan. Sagittal and coronal slices of two-ch lateral WECOT-BC and two-ch lateral CBC were given in the left-hand side and in the right-hand side, respectively. MR images of each phantom were demonstrated in the same row. The SNR maps were presented under the corresponding reception profiles.

Table 4.2 The measured impedance of the coils, ZS, ZM, and ZL, when they were loaded with S-BP, M-BP, and L-BP, respectively and the corresponding frequency shift

Coil	Channel#	Z_S (Ω)	Z_M (Ω)	Z_L (Ω)
Two-ch Lateral WECOT-BC	1	7-j12	9+j3	11+j17
	2	5-j14	7-j4	11+j12
	Δf (MHz)	8	Center	7
Two-ch Lateral CBC	1	6-j4	8-j3	10-j2
	2	3-j3	4-j2	6-j1
	Δf (MHz)	1.5	Center	2
Four-ch Bilateral WECOT-BC	1	7-j12	9+j3	11+j17
	2	5-j14	7-j4	11+j12
	3	7-j12	9-j2	12+j14
	4	7-j14	10-j3	12+j15
	Δf (MHz)	8	Center	7

The reception profile having the highest SNR among overall reception profiles of two-ch lateral WECOT-BC belonged to S-BP. The maximum SNR of B and O in sagittal slice of S-BP, followed by that of M-BP and L-BP, respectively. In other words, SNR of O in the sagittal slice of S-BP was approximately more than twice that of M-BP and L-BP. On the other hand, a signal loss in L and R was evident in all sagittal slices. While right-hand side of the coronal slices had higher SNR than left-hand side, SNR decreased from M-BP and L-BP.

Two-ch lateral CBC provided quite homogenous reception profile whose SNR was 120, in all slices except the sagittal slice of M-BP. SNR decreased in O of the sagittal slice of M-BP.

Sagittal slices of four-ch bilateral WECOT-BC (Fig. 4.6) corresponded to those of two-ch lateral WECOT-BC in terms of SNR distribution throughout the slice except the magnitude. On the other hand, SNR maps of coronal slices of phantoms demonstrated better reception profiles. However, coronal slices had asymmetric reception profiles such that right phantom had higher SNR throughout the slice than left phantom.

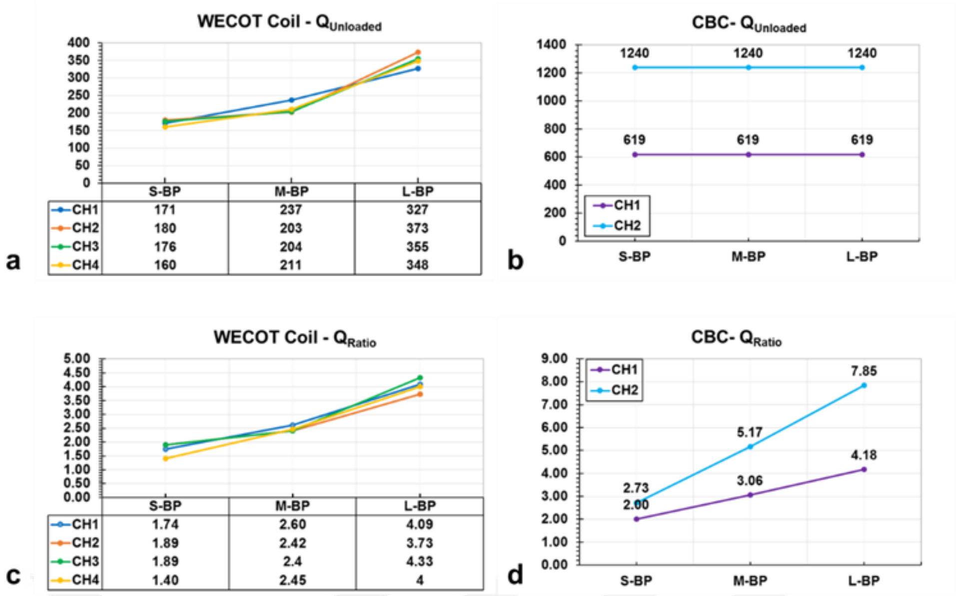

Figure 4.4 $Q_{Unloaded}$ and Q_{Ratio} graphs of WECOT-BC and CBC. (a) $Q_{Unloaded}$ results of Ch1-4 of WECOT-BC when it was on S-BP, M-BP, and L-BP. All values were given as data table below the graph. (b) $Q_{Unloaded}$ results of Ch1 and Ch2 of CBC when it was loaded with S-BP, M-BP, and L-BP. (c) Q_{Ratio} results of each channel of WECOT-BC when it was on S-BP, M-BP, and L-BP. The corresponding Q_{Ratio} values were given as data table below the graph. (d) Q_{Ratio} results of Ch1 and Ch2 of CBC when it was loaded with S-BP, M-BP, and L-BP

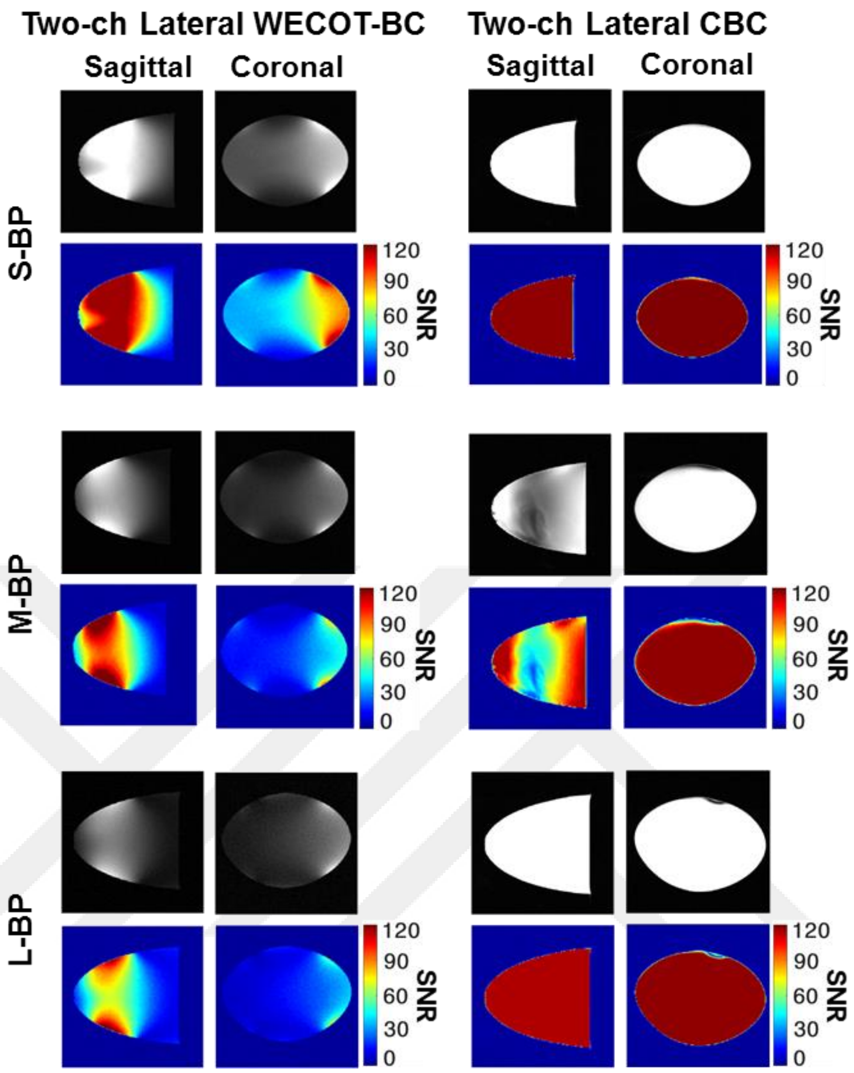

Figure 4.5 Sagittal and coronal reception profiles of two-ch lateral WECOT-BC and two-ch lateral CBC and their corresponding SNR maps when they were loaded with S-BP, M-BP, and L-BP

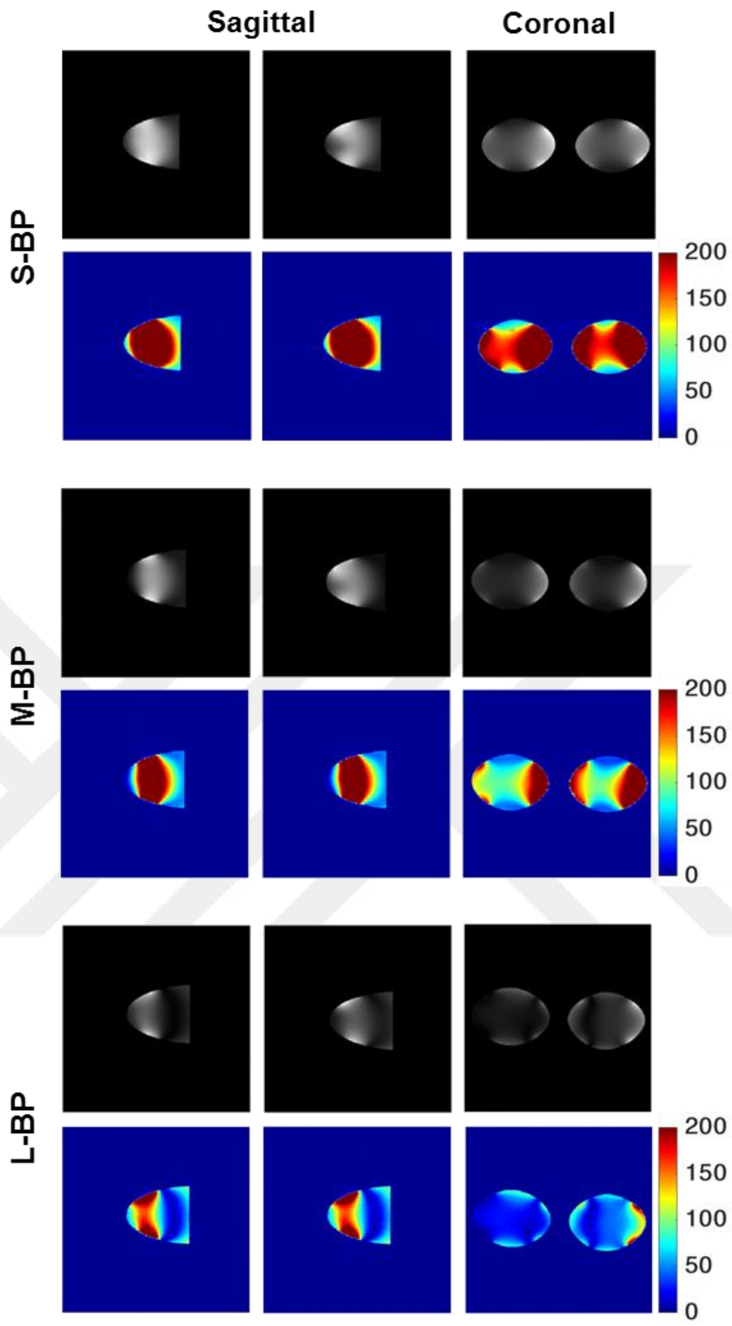

Figure 4.6 Sagittal and coronal reception profiles of four-ch bilateral WECOT-BC their corresponding SNR maps when it was loaded with S-BP, M-BP, and L-BP

4.3.3 Resolution Plate

The dimensions of the pattern in Fig. 4.3b were considered to evaluate the resolution performance of the coils. Figure 4.7 demonstrates MR images of resolution plate placed inside three phantoms. Each row contains the resolution plate images of the same phantom. Unprocessed resolution plate images of two-ch lateral WECOT-BC entitled as original and their enlarged views and corrected versions are given in the left-hand side. Resolution plate images of two-ch lateral CBC did not be in need of any correction since they were quite clear.

The letter S2 and four individual holes were easily distinguishable at the bottom of all sagittal slices of two-ch lateral WECOT-BC. Additionally, while 0.25 and 0.5 mm of lines, 1 mm and 2 mm element of the pattern were quite noticeable, 0.25 mm and 0.5 mm of holes were not observable clearly in this region (See enlarged views). 0.25 and 0.5 mm of lines could be recognized at the center and at the top of sagittal slice of S-BP. On the other hand, only those at the center of sagittal slice of M-BP and L-BP were discernable. The letter C1, four individual holes, all lines of the pattern, 0.5 mm, 1 mm, and 2 mm of holes could be distinguishable in all coronal slices of two-ch lateral WECOT-BC, but 0.25 mm of hole was not observable.

Sagittal and coronal slices of two-ch lateral CBC were superior to those of two-ch lateral WECOT-BC in terms of resolution capability. The letters S2 and C1, four individual holes, and the whole pattern were recognizable in all slices despite the inhomogeneous profile of sagittal slice of S phantom. Nevertheless, note that 0.25 mm of holes were hard to discern.

Resolution plate images obtained by four-ch bilateral WECOT-BC are given in Figure 4.8. The slices are grouped in three major rows. Each row of the phantom is consisted of two sub rows for original and corrected images. Two sagittal slices were acquired, the first was from the left phantom and the second belonged to the right phantom. FOV was adjusted to acquire coronal slices of both phantoms. Four individual holes, 1 mm and 2 mm element of the pattern were recognizable clearly in all slices of S-BP and M-BP. Four individual holes except 2 mm of hole, 1 mm and 2 mm element of the pattern were observable in all slices of L-BP. Yet, the letter S2 and C1, 0.5 mm and 0.25 mm element of the pattern were not easily distinguishable in all phantoms.

Overall assessment of sagittal and coronal slices demonstrated that the minimum resolution provided by two-ch lateral WECOT-BC and four-ch bilateral WECOT-BC was 0.25 mm and 1 mm in all phantoms, respectively. Corrected images of S-BP and M-BP provided significant improvements in the regions where two-ch lateral WECOT-BC and four-ch bilateral WECOT-BC were inadequate to receive signal, yet the same improvement could not be accomplished in those of L-BP.

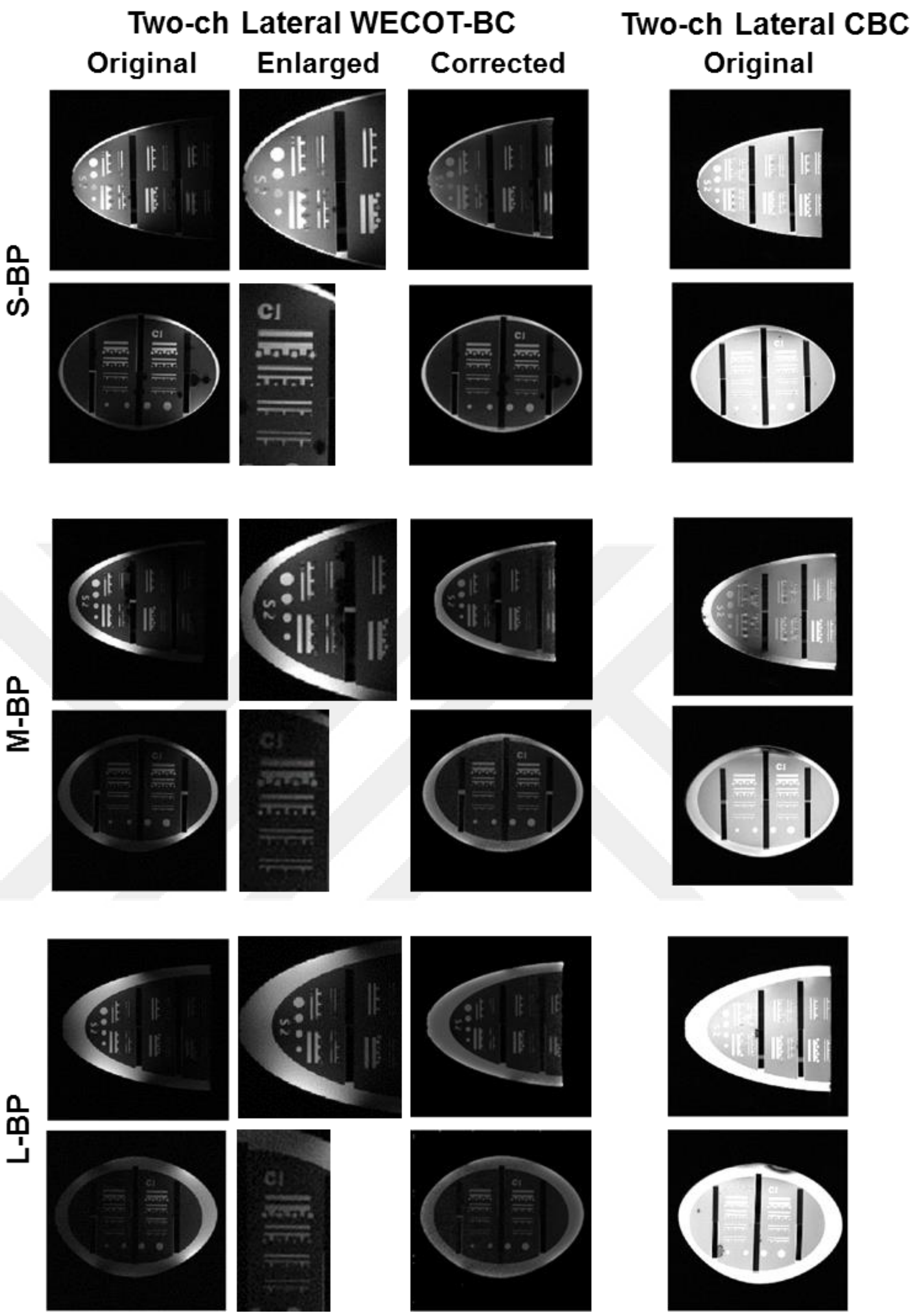

Figure 4.7 Sagittal and coronal slices of the resolution plate, their enlarged views, and their corrected versions using the corresponding reception profile

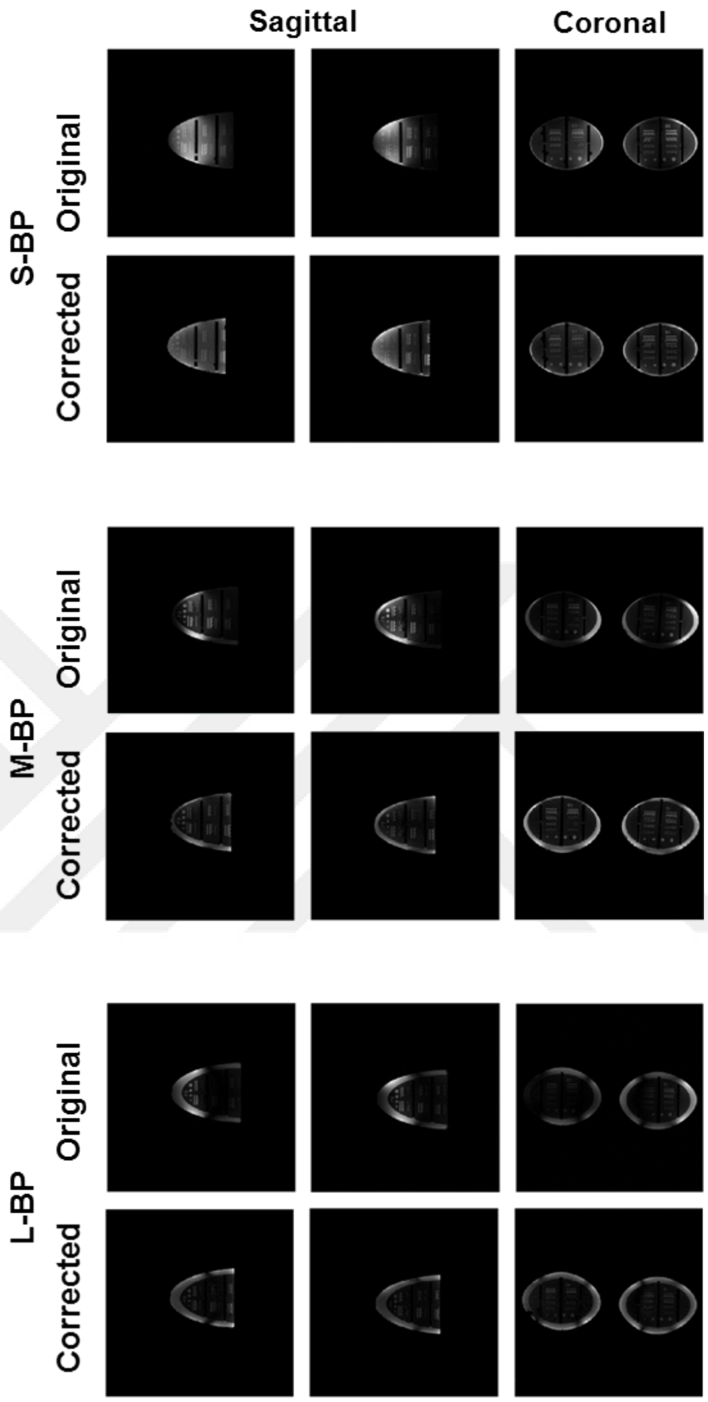

Figure 4.8 Sagittal and coronal slices of resolution plate setup acquired by 4-ch bilateral WECOT-BC. The corrected versions of the images is under the originals

4.4 Conclusion

Despite little volume difference among phantoms, the resultant frequency shift was too much to be compensated by a conventional matching technique used in coil designs. 3-stage matching could tolerate up to 16 Ω of reactance change, 20 nH of inductance change, and approximately 16 MHz of frequency shift. 3-stage broad-band matching of WECOT coil might result in that Q_{Loaded} values remained in 80-115 range in all phantoms. $Q_{Unloaded}$ values are constant in conventional coils since they have a fixed target volume. It is the amount of loading which determines Q_{Ratio}. On the contrary, WECOT coil demonstrated different $Q_{Unloaded}$ values in three phantoms and held the loading almost constant regardless of the size of the phantom. In the end, Q_{Ratio} corresponded with the size of the phantom, demonstrating the same behavior as a conventional coil.

Taking the regions with high SNR in the reception profiles of two-ch WECOT coil (Fig. 4.6) into account, it was notable that these regions had the same resolution (Fig. 4.7) as those of two-ch CBC. Additionally, in spite of relatively low SNR in L-BP images of two-ch WECOT coil, 0.25 mm of resolution was achieved as well. Considering DCIS detected in MRI may range from 5-67 mm (Rahbar et al., 2015), minimum resolution obtained by two-ch WECOT coil and four-ch WECOT coil was applicable in clinics. SNR maps of four-ch WECOT coil improved and their numerical value increased compared to those of two-ch WECOT coil, although they were in fact the same coil. The reason for difference was the increased FOV during four-ch WECOT coil acquisition. The increased FOV decreased the resolution obtained by four-ch WECOT coil conversely.

This study had some limitations. Even though the ability of the proposed CU saddle coil geometry to create a magnetic field that could penetrate homogenously inside the phantom was validated by two-ch CBC, WECOT coil failed to create the magnetic field with the same effect. Note that the conductivity of the coil material and sample are one of the primary noise sources of an MR image. Considering sample was held constant in the phantom setup, high DC resistivity of WECOT coil may dominate the resistance and resulted in inhomogeneous B_1^- field and low SNR. Nevertheless, the achieved resolution in Fig. 4.7 may infer that enhancing magnetic field of WECOT coil can also improve SNR and resolution. The first approach to enhance the magnetic field would be decreasing the target volume. It was standing out that low SNR in L-BP images of two-ch WECOT coil (Fig. 4.6) correlated with high resistance measured on L-BP (Table 4.2). Removing L-BP and replacing it with a phantom whose volume is 20% smaller (500 mL) than that of S-BP can provide high SNR because the expected coil resistance might decrease. The second approach would be increasing the conductivity of WECOT by reducing the amount of nonconductive elastofiber in the production process. Although the resultant elasticity of WECOT may decrease, it would be elastic enough to wear the phantoms.

CHAPTER 5

CONCLUSION

This thesis described a wearable receive-only ^{1}H loop coil, a transceiver ^{23}Na WECOT breast coil, a four-channel bilateral receive-only ^{1}H WECOT breast coil, and a two-stage LNA. The production technique of WECOT provided not only flexibility in determining the width of the textile and the percentage of elasticity, but also simplicity in creating the textile coil such as ability to be cut in desired length and to be sewn. The wearable receive-only ^{1}H loop coil was highly elastic such that it was compatible with a phantom whose dimension was 50% bigger than the previous size. On the other hand, the design of the circuit maintaining the matching for such a great inductance change resulted in relatively low mean SNR in the phantom images. The adjustability of the transceiver ^{23}Na WECOT breast coil with different sized phantoms was validated by the corresponding Q_{Ratio} values. In addition, the coil yielded correct concentration estimation in the regions with high sensitivity. Three-stage matching of the four-channel bilateral receive-only ^{1}H WECOT breast coil was able to tolerate approximately 16 MHz of frequency shift. Moreover, at least 0.25 mm of resolution was obtained. Two-stage LNA yielded 37 dB of gain could operate both at sodium and proton frequencies.

Future works will include the improvements in the production technique of WECOT, the design of a WECOT array coil, and the application of WECOT coils on other parts of the body.

REFERENCES

American Cancer Society. (2021). *Breast Cancer Facts & Figures*. Atlanta: American Cancer Society

Bangerter, N. K., Kaggie, J. D., Taylor, M. D., & Hadley, J. R. (2016). Sodium MRI radiofrequency coils for body imaging. *Nmr in Biomedicine*, *29*(2), 107-118.

Brown, R., Madelin, G., Lattanzi, R., Chang, G., Regatte, R. R., Sodickson, D. K., et. al. (2013). Design of a nested eight-channel sodium and four-channel proton coil for 7T knee imaging. *Magnetic Resonance in Medicine, 70*(1), 259-268.

Brown, R., Storey, P., Geppert, C., McGorty, K., Leite, A. P. K., Babb, J., et. al. (2014). Breast MRI at 7 Tesla with a bilateral coil and robust fat suppression. *Journal of Magnetic Resonance Imaging, 39*(3), 540-549.

By, S., Rispoli, J. V., Cheshkov, S., Dimitrov, I., Cui, J. M., Seiler, et.al. (2014). A 16-Channel Receive, Forced Current Excitation Dual-Transmit Coil for Breast Imaging at 7T. *Plos One*, *9*(11), e113969.

Corea, J. R., Flynn, A. M., Lechene, B., Scott, G., Reed, G. D., Shin, P. J., et. al. (2016). Screen-printed flexible MRI receive coils. *Nature Communications, 1-7*.

Doty, F. D., Connick, T. J., Ni, X. Z., & Clingan, M. N. (1988). Noise in high-power, high-frequency double-tuned probes. *Journal of Magnetic Resonance, 77*(3), 536-549.

Frass-Kriegl, R., de Lara, L. I. N., Pichler, M., Sieg, J., Moser, E., Windischberger, C., et. al. (2018). Flexible 23-channel coil array for high-resolution magnetic resonance imaging at 3 Tesla. *Plos One, 13*(11), e0206963.

Friedrich, M. (1998). MRI of the breast: state of the art. *European Radiology, 8*(5), 707-725.

Grabham, N. J., Li, Y., Clare, L. R., Stark, B. H., & Beeby, S. P. (2018). Fabrication techniques for manufacturing flexible coils on textiles for inductive power transfer. *Ieee Sensors Journal, 18*(6), 2599-2606.

Greenwood, H. I., Wilmes, L. J., Kelil, T., & Joe, B. N. (2020). Role of breast MRI in the evaluation and detection of DCIS: Opportunities and challenges. *Journal of Magnetic Resonance Imaging, 52*(3), 697-709.

Hanahan, D., & Weinberg, R. A. (2000). The hallmarks of cancer. *Cell, 100*(1), 57-70.

Hancu, I., Fiveland, E., Park, K., Giaquinto, R. O., Rohling, K., & Wiesinger, F. (2016). Flexible, 31-channel breast coil for enhanced parallel imaging performance at 3T. *Magnetic Resonance in Medicine, 75*(2), 897-905.

Heywang-Kobrunner, S. H., Hacker, A., & Sedlacek, S. (2013). Magnetic resonance imaging: The evolution of breast imaging. *Breast, 22*, 77-82.

Hornak, J. P., Szumowski, J., & Bryant, R. G. (1987). Elementary single turn solenoids used as the transmitter and receiver in magnetic-resonance-imaging. *Magnetic Resonance Imaging, 5*(3), 233-237.

Ianniello, C., Madelin, G., Lakshmanan, K., Zhang, B., Moy, L., & Brown, R. (2017). Design and performance of a dual tuned 7 T proton/sodium breast coil. *2017 International Conference on Electromagnetics in Advanced Applications (Iceaa)*, 1890-1893.

Insko, E. K., Connick, T. J., Schnall, M. D., & Orel, S. G. (1997). Multicoil array for high resolution imaging of the breast. *Magn Reson Med, 37*(5), 778-784.

Jacobs, M. A., Ouwerkerk, R., Wolff, A. C., Gabrielson, E., Warzecha, H., Jeter, S., et. al. (2011). Monitoring of neoadjuvant chemotherapy using multiparametric, Na-23 sodium MR, and multimodality (PET/CT/MRI) imaging in locally advanced breast cancer. *Breast Cancer Research and Treatment, 128*(1), 119-126.

Jacobs, M. A., Ouwerkerk, R., Wolff, A. C., Stearns, V., Bottomley, P. A., Barker, P. B., et. al. (2004). Multiparametric and multinuclear magnetic resonance imaging of human breast cancer: Current applications. *Technology in Cancer Research & Treatment, 3*(6), 543-550.

Kaggie, J. D., Hadley, J. R., Badal, J., Campbell, J. R., Park, D. J., Parker, D. L., et. al. (2014). A 3 T sodium and proton composite array breast coil. *Magnetic Resonance in Medicine, 71*(6), 2231-2242.

Kahraman-Agir, B., Bayrambas, B., Yegin, K., & Ozturk-Isik, E. (2019). Wearable and stretchable surface breast coil. *International Society for Magnetic Resonance in Medicine*, Montreal, Canada, 1501.

Kahraman-Agir, B., Bayrambas, B., Yegin, K., & Ozturk-Isik, E. (2020). A Wearable and flexible 23Na transmit/receive breast coil at 3T. *International Society for Magnetic Resonance in Medicine*, Virtual Meeting, 4104.

Kahraman-Agir, B., Yegin, K., & Ozturk-Isik, E. (2021). Wearable and elastic surface coil for 1H magnetic resonance imaging. *Ieee Microwave and Wireless Components Letters, 31*(5), 517-520.

Kim, J., Santini, T., Bae, K. T., Krishnamurthy, N., Zhao, Y. J., Zhao, T. J., et. al. (2017). Development of a 7 T RF coil system for breast imaging. *NMR in Biomedicine, 30*(1-10).

Kuhl, C. K., Mielcareck, P., Klaschik, S., Leutner, C., Wardelmann, E., Gieseke, J., et. al. (1999). Dynamic breast MR imaging: are signal intensity time course data useful for differential diagnosis of enhancing lesions? *Radiology, 211*(1), 101-110.

Madelin, G., Lee, J. S., Regatte, R. R., & Jerschow, A. (2014). Sodium MRI: Methods and applications. *Progress in Nuclear Magnetic Resonance Spectroscopy, 79*, 14-47.

Mann, R. M., Cho, N., & Moy, L. (2019). Breast MRI: State of the Art. *Radiology, 292*(3), 520-536.

Mann, R. M., Kuhl, C. K., & Moy, L. (2019). Contrast-enhanced MRI for breast cancer screening. *Journal of Magnetic Resonance Imaging, 50*(2), 377-390.

Marino, M. A., Helbich, T., Baltzer, P., & Pinker-Domenig, K. (2018). Multiparametric MRI of the breast: A review. *Journal of Magnetic Resonance Imaging, 47*(2), 301-315.

McDougall, M. P., Cheshkov, S., Rispoli, J., Malloy, C., Dimitrov, I., & Wright, S. M. (2014). Quadrature transmit coil for breast imaging at 7 Tesla using forced current excitation for improved homogeneity. *Journal of Magnetic Resonance Imaging, 40*(5), 1165-1173.

McGhee, D. E., & Steele, J. R. (2011). Breast volume and bra size. *International Journal of Clothing Science and Technology, 23*(5), 351-360.

Mcowan, P. W., & Redpath, T. W. (1987). A specialized receiver coil for NMR imaging of female breasts. *Physics in Medicine and Biology, 32*(2), 259-263.

Mispelter, Joe l, Lupu, Mihaela, & Briguet, Andre. (2006). *NMR probeheads for biophysical and biomedical experiments : Theoretical principles & practical guidelines*. London: Imperial College Press.

Mussurakis, S., Buckley, D. L., & Horsman, A. (1997). Prediction of axillary lymph node status in invasive breast cancer with dynamic contrast-enhanced MR imaging. *Radiology, 203*(2), 317-321.

Nnewihe, A. N., Grafendorfer, T., Daniel, B. L., Calderon, P., Alley, M. T., Robb, F., et. al. (2011). Custom-fitted 16-channel bilateral breast coil for bidirectional parallel imaging. *Magnetic Resonance in Medicine, 66*(1), 281-289.

Nordmeyer-Massner, J. A., De Zanche, N., & Pruessmann, K. P. (2012). Stretchable coil arrays: Application to knee imaging under varying flexion angles. *Magnetic Resonance in Medicine, 67*(3), 872-879.

Ojeda-Fournier, H., Choe, K. A., & Mahoney, M. C. (2007). Recognizing and interpreting artifacts and pitfalls in MR imaging of the breast. *Radiographics, 27*, S147-S164.

Ouwerkerk, R., Jacobs, M. A., Macura, K. J., Wolff, A. C., Stearns, V., Mezban, S. D., et. al. (2007). Elevated tissue sodium concentration in malignant breast lesions detected with non-invasive Na-23 MRI. *Breast Cancer Research and Treatment, 106*(2), 151-160.

Pethig, R., & Kell, D. B. (1987). The Passive Electrical-Properties of Biological-Systems - Their Significance in Physiology, Biophysics and Biotechnology. *Physics in Medicine and Biology, 32*(8), 933-970.

Port, A., Luechinger, R., Albisetti, L., Varga, M., Marjanovic, J., Reber, J., et. al. (2020). Detector clothes for MRI: A wearable array receiver based on liquid metal in elastic tubes. *Scientific Reports, 10:8844*.

Port, A., Luechinger, R., Brunner, D. O., & Pruessmann, K. P. (2021). Elastomer coils for wearable MR detection. *Magnetic Resonance in Medicine, 85*(5), 2882-2891.

Rahbar, H., DeMartini, W. B., Lee, A. Y., Partridge, S. C., Peacock, S., & Lehman, C. D. (2015). Accuracy of 3 T versus 1.5 T breast MRI for pre-operative assessment of extent of disease in newly diagnosed DCIS. *European Journal of Radiology, 84*(4), 611-616.

Rankin, S. C. (2000). MRI of the breast. *British Journal of Radiology, 73*(872), 806-818.

Republic of Turkey Ministry of Health. (2021). *General Directorate of Public Health Turkey Cancer Statistics for 2016*. Ankara: Republic of Turkey Ministry of Health.

Shin, J., Kim, M. J., Lee, J., Nam, Y., Kim, M. O., Choi, N., et. al. (2015). Initial study on in vivo conductivity mapping of breast cancer using MRI. *Journal of Magnetic Resonance Imaging, 42*(2), 371-378.

Siegel, R. L., Miller, K. D., & Jemal, A. (2020). Cancer statistics, 2020. *Ca-a Cancer Journal for Clinicians, 70*(1), 7-30.

Ulaby, F.T., Michielssen, E., & Ravaioli, U. (2015). *Fundamentals of Applied Electromagnetics*. London: Pearson Education.

Vasanawala, S. S., Stormont, R., Lindsay, S., Grafendorfer, T., Cheng, J.Y., Pauly, J.M., et al. (2017). Development and clinical implementation of very light weight and highly flexible AIR technology arrays. *International Society for Magnetic Resonance in Medicine*, Honolulu, USA, 0755.

Vaughan, J.T., & Griffiths, J.R. (2012). *RF Coils for MRI*. West Sussex: Wiley.

Vincent, J. M., & Rispoli, J. V. (2020). Conductive thread-based stretchable and flexible radiofrequency coils for magnetic resonance imaging. *Ieee Transactions on Biomedical Engineering, 67*(8), 2187-2193.

Wang, J. M., Reykowski, A., & Dickas, J. (1995). Calculation of the signal-to-noise ratio for simple surface coils and arrays of coils. *Ieee Transactions on Biomedical Engineering, 42*(9), 908-917.

Winkler, S. A., Corea, J., Lechene, B., O'Brien, K., Bonanni, J. R., Chauelhari, A., et. al. (2019). Evaluation of a flexible 12-channel screen-printed pediatric MRI coil. *Radiology, 291*(1), 179-184.

Wolfman, N. T., Moran, R., Moran, P. R., & Karstaedt, N. (1985). Simultaneous MR imaging of both breasts using a dedicated receiver coil. *Radiology, 155*(1), 241-243.

World Health Organization. (2021). *Cancer*. Retrieved June 19, 2021, from https://www.who.int/news-room/fact-sheets/detail/cancer

Zhang, B., Brown, R., Cloos, M., Lattanzi, R., Sodickson, D., & Wiggins, G. (2019). Size-adaptable "Trellis" structure for tailored MRI coil arrays. *Magnetic Resonance in Medicine, 81*(5), 3406-3415.

Zhang, B., Sodickson, D. K., & Cloos, M. A. (2018). A high-impedance detector-array glove for magnetic resonance imaging of the hand. *Nature Biomedical Engineering, 2*(9), 708-708.

Zhang, D. S., & Rahmat-Samii, Y. (2017). Flexible RF coil array system utilizing electro-textiles for 3t mri carotid artery imaging. *2017 Ieee International Symposium on Antennas and Propagation & Usnc/Ursi National Radio Science Meeting*, 1015-1016.

Zhang, T., Grafendorfer, T., Cheng, J. Y., Ning, P. G., Rainey, B., Giancola, M., et. al. (2016). A Semiflexible 64-Channel Receive-Only Phased Array for Pediatric Body MRI at 3T. *Magnetic Resonance in Medicine, 76*(3), 1015-1021.